A PHASE SPACE BEAM POSITION MONITOR FOR SYNCHROTRON RADIATION

A Dissertation Submitted to

the College of Graduate Studies and Research

in Partial Fulfillment of the Requirements

for the Degree of Master of Science

in the

Division of Biomedical Engineering

College of Engineering

University of Saskatchewan

By

Nazanin Samadi

Saskatoon, SK

Canada

PERMISSION TO USE

In presenting this thesis in partial fulfilment of the requirements for a Postgraduate degree from the University of Saskatchewan, I agree that the Libraries of this University may make it freely available for inspection. I further agree that permission for copying of this thesis in any manner, in whole or in part, for scholarly purposes may be granted by the professor or professors who supervised my thesis work or, in their absence, by the Head of the Department or the Dean of the College in which my thesis work was done. It is understood that any copying or publication or use of this thesis or parts thereof for financial gain shall not be allowed without my written permission. It is also understood that due recognition shall be given to me and to the University of Saskatchewan in any scholarly use which may be made of any material in my thesis.

Requests for permission to copy or to make other use of material in this thesis in whole or part should be addressed to:

Head of the Division of Biomedical Engineering

University of Saskatchewan

57 Campus Drive

Saskatoon, Saskatchewan, S7N 5A9

ABSTRACT

The stability of the photon beam position on synchrotron beamlines is critical for most if not all synchrotron radiation experiments. On wiggler and bend magnet beamlines, the vertical position is most critical due to the large horizontal width of the beam. The position of the beam at the experiment or optical element location is set by the position and trajectory of the electron beam source as it traverses the magnetic field of the bend magnet or the insertion device. Thus an ideal photon beam monitor would be able to simultaneously measure the photon beam's vertical position and angle, or its position in phase space.

X-ray diffraction is commonly used to prepare a monochromatic beam on x-ray beamlines usually in the form of a double crystal monochromator using perfect crystals. Diffraction from crystals couples the photon wavelength or energy to the incident angle on the crystal or lattice planes within the crystal. A monochromatic beam from such a monochromator will contain a spread of energies due to the vertical divergence of the photon beam from the source. This range of energies can easily cover the absorption edge of an element such as iodine at 33.17keV. It has been found that a system composed of a double crystal monochromator and an iodine filter that horizontally covers part of the monochromatic beam and an imaging detector can be used to independently and simultaneously measure the position and angle of the photon beam. This information can then be translated back to determine the vertical position and angle, or vertical phase space, of the electron beam source. This approach to measurement of the phase space of the source has not been done before and thus this study is the first of its kind.

The goal of this thesis is to investigate the use of this combined monochromator, filter and detector as a phase space beam position monitor. The system was tested for sensitivity to position and angle under a number of synchrotron operating conditions (normal operations and

special operating modes where the beam is intentionally altered in position and angle). These results were compared to other methods of beam position measurement from the literature to assess the utility of such a system as a beam diagnostic, a feedback element for electron beam control and a source of information that could be used to correct the experimental data to account for beam position and angle motion.

ACKNOWLEDGEMENTS

First and most of all, I would like to express my deepest gratitude to my supervisor, Prof. Dean Chapman for his continuous support during my studies and the writing this thesis. He inspired me with his knowledge, passion and smile and gave me freedom in my research. He made me fall in love with physics, and nature. He not only guided me throughout my research, but also he taught me a better way to see the world and try to be a better person. I could not wish for a better and friendlier supervisor. Also, I want to thank Dean and his great family for filling the absence of my own family here in Canada.

Special thanks to my advisory committee, Dr. Mark de Jong and Dr. David Cooper, for their great ideas, knowledge and input into this work. It was a great pleasure to have them as my advisors and be able to use their guidance throughout my program.

I also would like to thank Dr. Les Dallin for his help and support during my experiments, helping me for hours to collect data and having a lots of input into this work.

I thank Dr. George Belev and the rest of the BMIT staff at the Canadian Light Source for their great guidance and help during my experiments and research.

Thanks go to my colleagues Mercedes Martinson and Bassey Bassey for their support and help in my research and also for being great friends.

My warmest thanks to all of my friends. Each of them opened a new window for me to look at the world with their amazing personalities. Also a lot of thanks go to Ashkan who helped me a lot in formatting this thesis.

I also wish to acknowledge the financial support of Canadian Institutes of Health Research (CIHR) Training Grant - Training in Health Research Using Synchrotron Techniques, Saskatchewan Health Research Foundation Team Grant, Natural Sciences and Engineering

Research Council of Canada (NSERC) Discovery Grant, the University of Saskatchewan, and Canada Research Chair Program. Research described in this thesis was performed at the Canadian Light Source, which is funded by the Canada Foundation for Innovation, NSERC, the National Research Council Canada, CIHR, the Government of Saskatchewan, Western Economic Diversification Canada, and the University of Saskatchewan.

I finish with my amazing family, my parents and my sisters, for their unconditional support and motivation. I want to thank them for never stopping believing in me. I'm grateful to have them.

To my beloved mom, dad and sisters

Ladan, Ahmad, Negin, Nasim and Naghmeh

And

To the bright memory of my loving grandparents

Azar joon and Baba jooni

TABLE OF CONTENTS

LIST OF TABLES

LIST OF FIGURES

ABBREVIATION

ACRONYMS

CLS	Canadian Light Source
BMIT	Biomedical Imaging and Therapy
DCM	Double crystal monochromator
DS	Development mode special beamline development
eBPM	Electron beam position monitor
IDL	Interactive Data Language (Exelis Visual Information Solutions)
KES	K-Edge subtraction
LINAC	linear accelerator
NS	Normal mode special beamline request/commissioning
OC	Orbit corrector
OSR	Optical synchrotron radiation
pBMP	Photon beam-position monitor
ps-BPM	Phase space – beam position monitor
RF	Radio frequency
XSR	X-ray Synchrotron Radiation

ENGLISH SYMBOLS

a_0	Cubic cell dimension
D	Distance from the source to the detector
d	Spacing between lattice planes (called the d-spacing)
E	Energy
E_{ring}	Electron beam energy

Fe	Iron
Gd	Gadolinium
hkl	Miller indices
I	Iodine
I	Intensity
K	Gain
$m_{\varepsilon}c^2$	Electron's rest mass energy
n	Diffraction order
P	Uncorrected orbit position
Pb	Lead
QA	Quadrupole type A
QB	Quadrupole type B
R	Response matrix
SB	Sextuple type B
Si	Silicon
SOA	Sextuple type A
t	Thickness
V_A	Electron beam induce Voltage eBPM button A
V_B	Electron beam induce Voltage eBPM button B
V_C	Electron beam induce Voltage eBPM button C
V_D	Electron beam induce Voltage eBPM button D
W	Tungsten
X	Position of the beam

Y	Position of the beam
x	Horizontal position of the electron beam source
y	Vertical position of the electron beam source
y'	Vertical angle of the electron beam source
y_c	Measured vertical K-edge position
y_d	Measured vertical beam position by the imaging detector
Z	Atomic number of the element

GREEK SYMBOLS

γ	Ratio of the electron beam energy to the electron's rest mass energy
ε_x	Horizontal electron beam emittance
ε_y	Vertical electron beam emittance
θ	Angle between the incident beam and lattice planes (Bragg angle)
λ	Wavelength
μ	linear attenuation coefficient
ρ	Mass density
ω_D	Darwin width

SUBSCRIPTS

div	divergence
int	intrinsic

CHAPTER 1

INTRODUCTION

1.1 INTRODUCTION

The propagation of light can be described from either a wave or ray point of view. In many instances a ray description is sufficient to define the path. In free space, the knowledge of the trajectory or a position in space and the direction of the ray at a time is sufficient to define where the light ray will be at any later time assuming that the ray is not absorbed or altered in energy. In a general sense, the direction of a ray or particle (photon) of light is best defined by the momentum. The combination of the position and momentum is commonly referred to as a "phase space" location [1]. Again for a system where the energy of the particle is not changed, the vector direction of the momentum can be described by two angles in some reference frame. Those two angles along with the spatial location are sufficient to define the phase space position. The trajectory or phase space position of a photon beam in a plane can be determined if both the position and angle in that plane can be found at some point along the propagation direction. From knowledge of the phase space position, it is possible to determine the photon beam position and angle at the source or at another location if the optics at the intervening positions and their effects are known.

This thesis describes a method to simultaneously measure the photon beam position and angle or phase space position in a plane at one location from a synchrotron source which was developed and tested at the Canadian Light Source (CLS) on the biomedical beamline.

The CLS is one of the world's third generation synchrotron facilities with a low electron beam emittance (ε_x = 15 nm-rad, ε_y = 200 pm-rad). Beam instability, be it electron or photon beam, can be a problem at synchrotron facilities, especially the third generation facilities; it has adverse effects on the required low electron beam emittance, effective brilliance of the synchrotron radiation, and experiments performed at the experimental stations [2-5]. The causes of beam instability and the methods of reduction have been widely studied [5-9], and the drive to ensure and maintain a steady beam has led to the development of different types of beam monitors [10-24].

Photon beam position and angle instabilities at experimental stations are attributed to fluctuations of the stored electron beam orbit as well as vibrational and thermal distortion of beamline optical components. The desired levels of stability in the vertical plane are 10% of the electron beam size in position and angle [6]. It has been reported that most of the available photon beam monitors are sensitive to position only, and hence are known as photon beam position monitors (PBPM). They do not provide any information about the photon beam angle stability [19, 25]; however, beam angle also needs to be monitored because of the negative effects of beam angle instability [19, 26-28]. The use of two PBPMs is common, when the angle of a photon beam is to be measured [19, 23, 24]. However, for accurate measurements the two monitors need to be separated by a considerable distance with little or no beam filtration, resizing or optics in between the monitors which tends to be impractical in most beamlines.

At the CLS, beam instabilities (modes, frequencies, rise time, etc.) are monitored by two diagnostic beamlines - the Optical Synchrotron Radiation (OSR) and the X-ray Synchrotron Radiation (XSR) beamlines [29]. Most beamlines at the CLS have provision for some type of beam position monitors, but few are actually implemented or used. These monitors are of the type that measure only the beam position at some location in the beamline.

Beam motion will affect almost all synchrotron experiments, but on an imaging beamline, these effects are quite noticeable. One of the imaging techniques being used at the CLS Biomedical Imaging and Therapy (BMIT) bend magnet beamline [30, 31] is a spectral K-Edge Subtraction (KES) imaging [32]. This system uses a bent Laue monochromator that has very good focal and energy dispersive properties for high resolution imaging of small animals usually the vasculature using iodated contrast agents. This monochromator provides a beam with about a 500 eV energy spread and can be tuned to a specific K-edge of an element giving around 250 eV above and below the K-edge. This system is sensitive to the spatial location of the K-edge. In one of the experiments with this system in December 2013 using iodine K-edge, we saw horizontal banding (Figure 1- 1) in the images that indicated that the photon beam was moving vertically. It was also noticed that in the regions that contained iodine the location of the K-edge moved a different amount than the photon beam motion. This observation led to the idea that maybe I can disentangle the photon beam phase space position by measuring the photon beam center as well as the edge location within that beam.

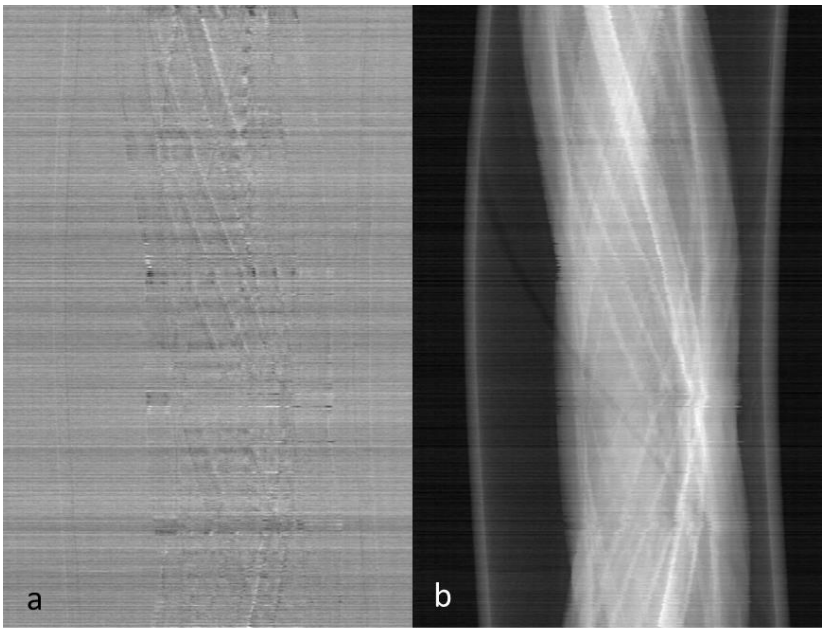

Figure 1- 1 An example of image banding due to beam motion, observed with Spectral KES system on CLS BMIT bend magnet beamline. Figure a is iodine contrast sinogram and b is the water equivalent sinogram. The banding appears as horizontal lines whose intensity vary from the top to the bottom of the figures.

Based on this observation I present a unique method for measuring the position and angle of a photon beam simultaneously – a Phase Space – Beam Position Monitor (ps-BPM). The method relies on the energy dispersive properties of x-ray diffraction from flat crystals and makes use of the absorption edge of an element to determine a specific energy or angle of the photon beam.

1.2 OBJECTIVE

The objective of this project was to determine the feasibility of a ps-BPM by:

1. Assembling a prototype system,
2. Developing a theory of operation,
3. Making measurements where the electrons in the storage ring were moved in position and angle to assess its performance,

4. Making measurements during normal operations of the storage ring,
5. Assessing the measurements in the context of other beam position monitors from the published literature, and
6. Publishing the results.

Based on the outcome of the results I would begin to consider possible designs of a dedicated system that could be used in a synchrotron beamline.

A brief introduction to synchrotron radiation, x-ray diffraction and absorption edges of elements are required to better understand the operation of the ps-BPM system.

1.3 SYNCHROTRON RADIATION

Synchrotron radiation is created when electrons are in circular motion at speeds close to that of light (relativistic electrons). The acceleration due to changes in the direction of the velocity vector in circular motion (centripetal acceleration) is responsible for the creation of light. Wherever the electrons are pointing as they are being transversely accelerated is where the light is emitted into a roughly 1/γ angle cone measured in radians[*]. Gamma (γ) is the ratio of the electron beam energy to the electron's rest mass energy ($\gamma = \frac{E_{ring}}{m_e c^2} = 5675$ for the CLS); 1/γ is commonly called the opening angle of the beam. A schematic of the radiation from a relativistic electron in circular motion is shown in Figure 1- 2.

[*] Sometimes ± 1/γ or a full range of 2/γ is used to represent the opening angle of the synchrotron beam. In this thesis we use 1/γ as the opening angle since most of the beam vertically falls within this angular range (see Figure 1-3).

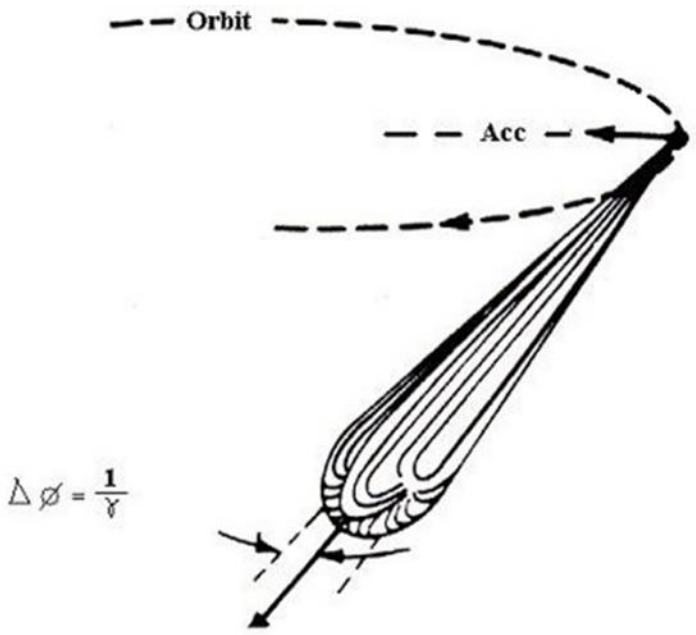

Figure 1- 2 Synchrotron radiation pattern from an electron transversely accelerated in uniform circular motion as would be the case in a bend magnet field. The photon beam follows the instantaneous trajectory of the electron. Image adapted from: http://upload.wikimedia.org/wikipedia/commons/d/de/Syncrotron_radiation_energy_flux.png

For the CLS, the opening angle of the radiation is 1/5675 radians or 176 microradians. The synchrotron beam has a vertical distribution that is nearly Gaussian but is properly described by a modified Bessel function of the second kind [33]. A measured comparison of the vertical distribution of the beam on the CLS BMIT bend magnet beamline is shown in Figure 1- 3 at 33.17 keV. As measured on a beamline some distance from the source, a vertical angle or position motion of the electron source will move this distribution vertically. Because the measurement distance from source can be tens of meters, the angle effects are amplified. For example, the profile measured in Figure 1- 3 is at 26 m from the electron beam source. In this figure the blue line is the measured profile from the image at the top of the figure. The red dashed line is a Gaussian fit to that profile. The fact that the red dashed line is hard to see indicates how closely the Gaussian fit is to the actual beam profile. The black dashed line is a calculated profile from modified Bessel function [33] for the actual conditions of the

measurement (CLS Bend Magnet [2.9 GeV & 1.354 T] at 26 m from the source with 100 μm pixels and 33.17 keV photon energy).

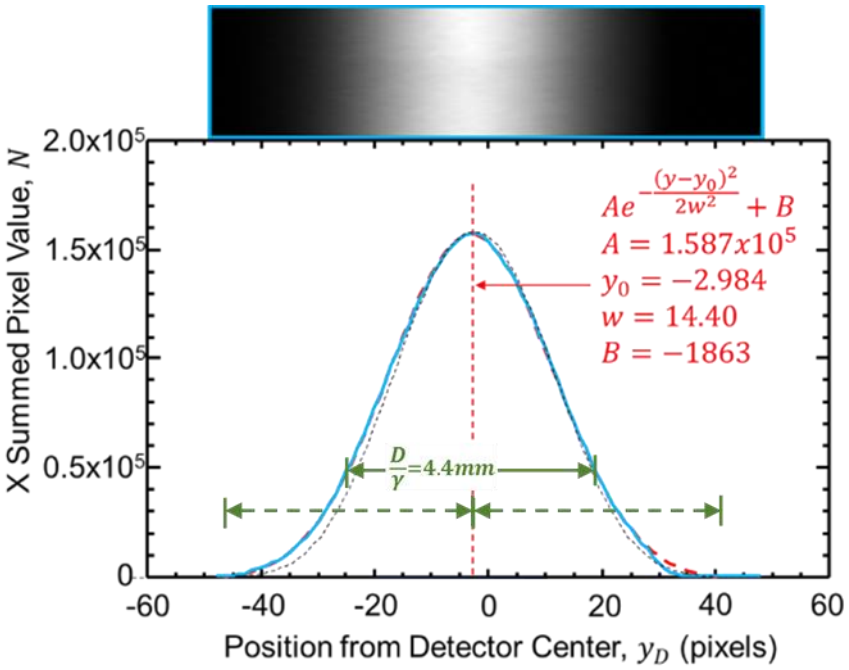

Figure 1- 3 Nearly Gaussian vertical beam profile as measured on the CLS BMIT bend magnet beamline. The picture at the top is an image of the beam rotated by 90 degrees to match the horizontal axis of the plot below. The plot at the bottom shows the measured beam profile from that image (blue) and a Gaussian fit (red dash). The red dotted line identifies the center. The red text gives the least squares Gaussian fitting parameters. The vertical scale is in pixel units (100 micron pixel size). The calculated beam profile is shown as the black dashed line. For reference the 1/γ beam width (25m×1/γ = 4.4mm) is indicated (solid green line) as well as ± 1/γ lines, also for reference (dashed green lines). As can be seen most of the beam is encompassed within the 1/γ range (~87% of the area under the curve or 31% of the peak value).

1.3.1 Description of the CLS

The Canadian Light Source (CLS) is a third generation synchrotron on the University of Saskatchewan campus in Saskatoon, SK, Canada. This 2.9 GeV electron beam energy storage ring became operational in 2004. The facility hosts 15 operational beamlines with two of the beamlines dedicated to monitoring the beam (OSR and XSR). See Figure 1- 4 which shows a layout of the facility. This work was done on the BMIT which is in the upper right of the figure.

The source of light for the facility is the storage ring, however there are two accelerators which are used to provide 2.9 GeV electrons and inject them into storage ring.

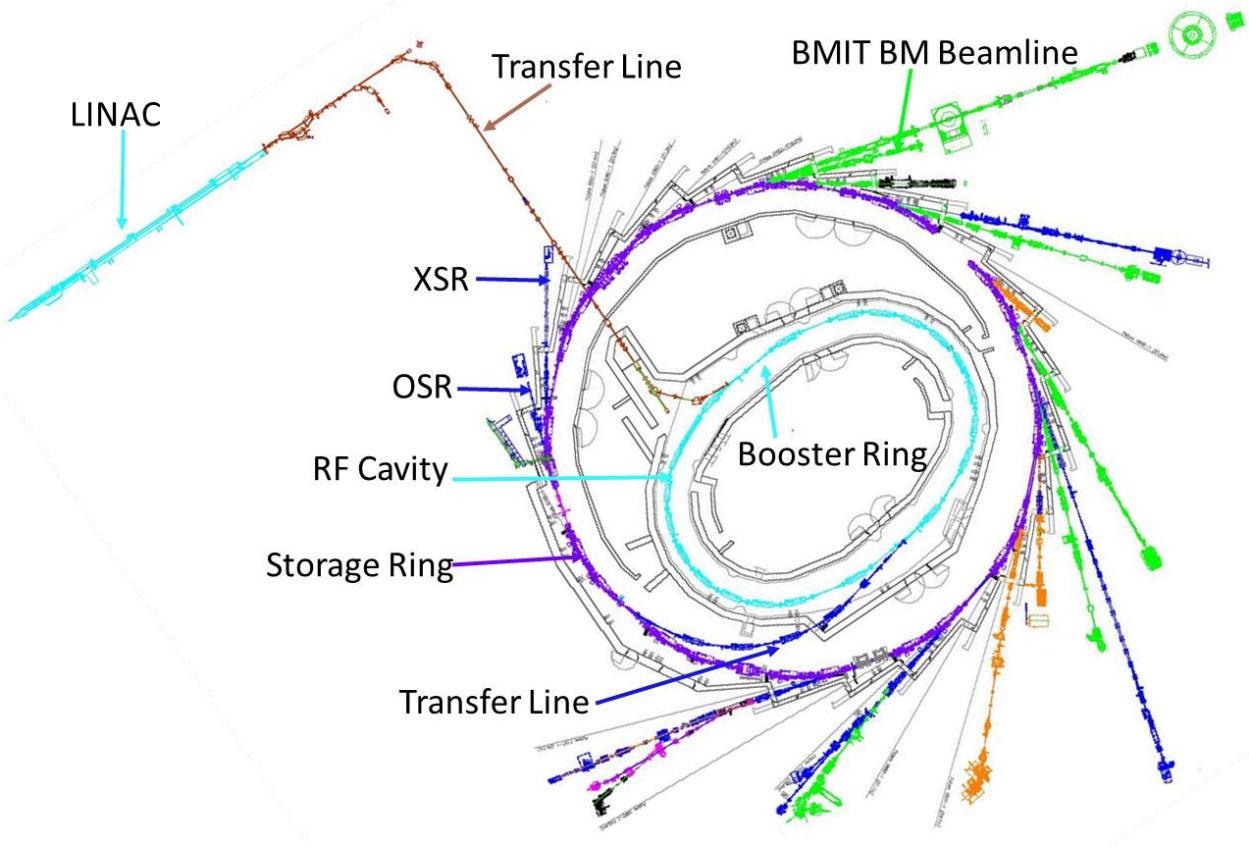

Figure 1- 4 Layout of the CLS accelerators, storage ring and beamlines. Image courtesy of Dr. Les Dallin, CLS

1.3.1.1 The Injection System

The initial acceleration of electrons occurs in a linear accelerator (LINAC) which is composed of a series of radio frequency cavities through which the electrons pass and gain energy. At the end of the LINAC the electrons have an energy of 300 MeV. These electrons are transported in evacuated pipes and directed with magnets to the booster synchrotron which is inside of the CLS storage ring. These accelerators are indicated in Figure 1- 4.

The 300 MeV electrons are injected into the booster synchrotron where they circulate in a racetrack-shaped orbit. The electrons are ramped in energy within the synchrotron by repeated

accelerations as they pass through an RF cavity while the magnetic field in the booster dipole magnets is synchronously ramped to maintain the same orbit. After the electrons attain the 2.9 GeV energy they are extracted from the synchrotron and injected to the storage ring.

1.3.1.2 Storage ring

The storage ring is optimized for the production of synchrotron light. The electrons circulate through a series of bending (dipole) and focusing (quadrupole and sextuple) magnets as well as devices designed to enhance synchrotron radiation for research purposes (insertion devices). Loss of electron beam energy due to synchrotron radiation is replaced by an RF cavity in the storage ring. There are three different families of quadrupoles (quads) which are all horizontally focusing. Each family type has 24 quads leading to a total of 72 quads in the storage ring.

The storage ring is made up of a repeating magnetic structure composed of 12 identical cells. A diagram of a cell is shown in Figure 1- 5. One cell is made up of two dipoles with a vertical field gradient used for vertical focusing. There are three families of two quads in each cell. These families used for horizontal focusing are designated QA, QB and QC. The cell also includes two sextupole families which correct for chromatic effects. These families are designated SOA and SB. The cell also includes four XY orbit corrector magnets (OCs). Two are standalone OCs and two are OCs built into the SOA sextupoles.

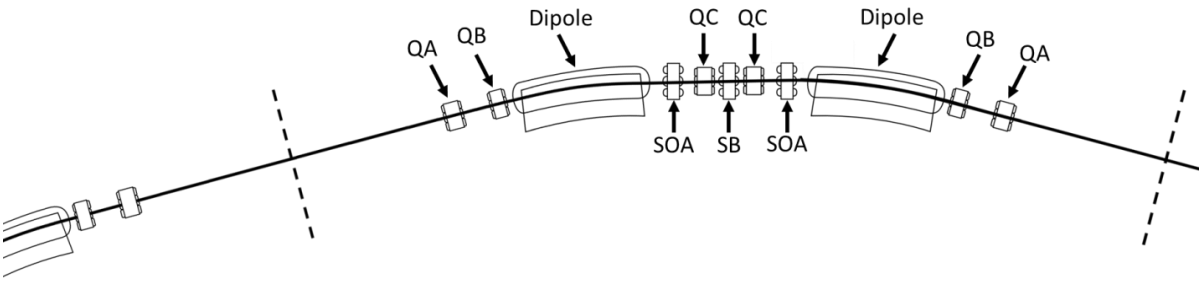

Figure 1- 5 Diagram showing the magnetic components in a CLS storage ring sector. The repeating unit of the sector is between the two dashed lines which is in the middle of the long insertion straights. The magnetic components labeled are described in the text.

1.3.1.3 Measurement and Control of the Electron Beam

Orbit stability is obtained by a feedback system in which the orbit is measured by electron beam position monitors (eBPM) and is corrected by orbit corrector magnets (OC). The eBPMs are structured in a way that they can measure both the vertical and horizontal position (see Figure 1- 6). The eBPM is composed of four buttons internal to the ring vacuum that sense the electron beam position.

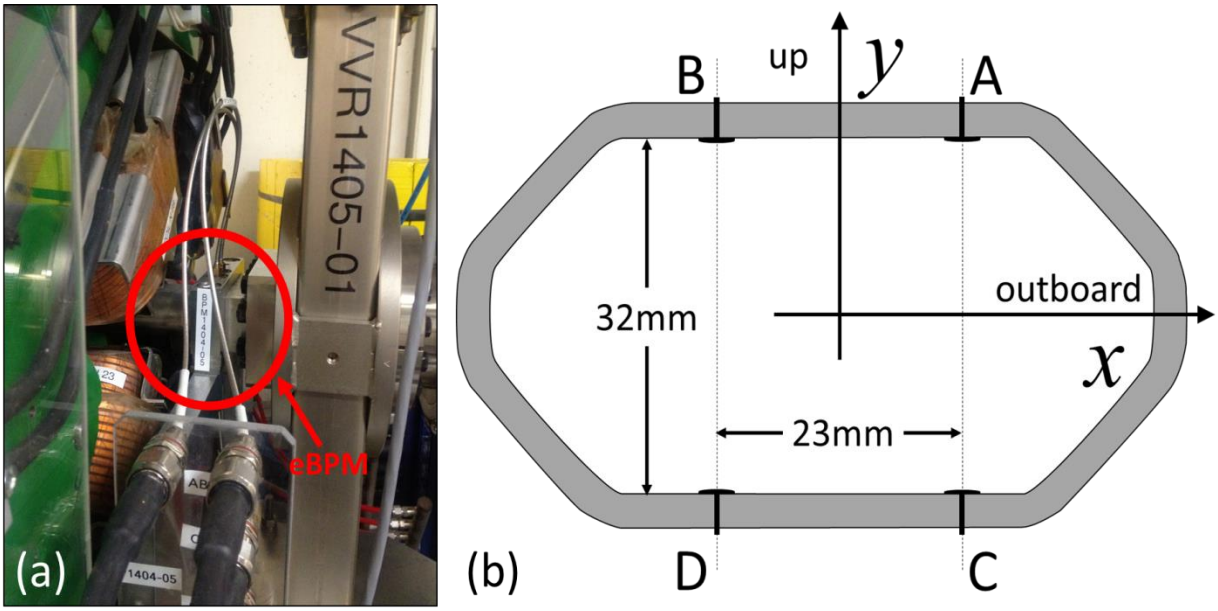

Figure 1- 6 Electron Beam Position Monitor (eBPM). Figure a shows an eBPM in the CLS storage ring and figure b shows a schematic of the eBPM four buttons along with some dimensions. Image (b) courtesy Dr. Dean Chapman.

There are two buttons on the top labeled A (outboard) and B (inboard) – see Figure 1- 6 (b). Similarly there are two buttons on the bottom: C (outboard) and D (inboard). The electron beam induces voltages on the four buttons; V_A, V_B, V_C and V_D. These signals are combined to give the horizontal, *X*, and the vertical, *Y*, position of the beam using,

$$X = K_x \frac{(V_B + V_D) - (V_A + V_C)}{V_A + V_B + V_C + V_D}, \quad (1.\ 1)$$

$$Y = K_y \frac{(V_A + V_B) - (V_C + V_D)}{V_A + V_B + V_C + V_D}, \quad (1.\ 2)$$

where, K_x is the horizontal gain and K_y is the vertical gain. With this system *X* is positive on the outboard side and up is positive for *Y* [34]. These types of the position sensors where four measurements are made to determine an *X* and *Y* location are commonly called the quadrant detectors.

The orbit correctors (OCs) are dipole electromagnets (see Figure 1- 7). There are pairs of dipoles; one for horizontal, *X*, and one for vertical, *Y* (see Figure 1- 7).

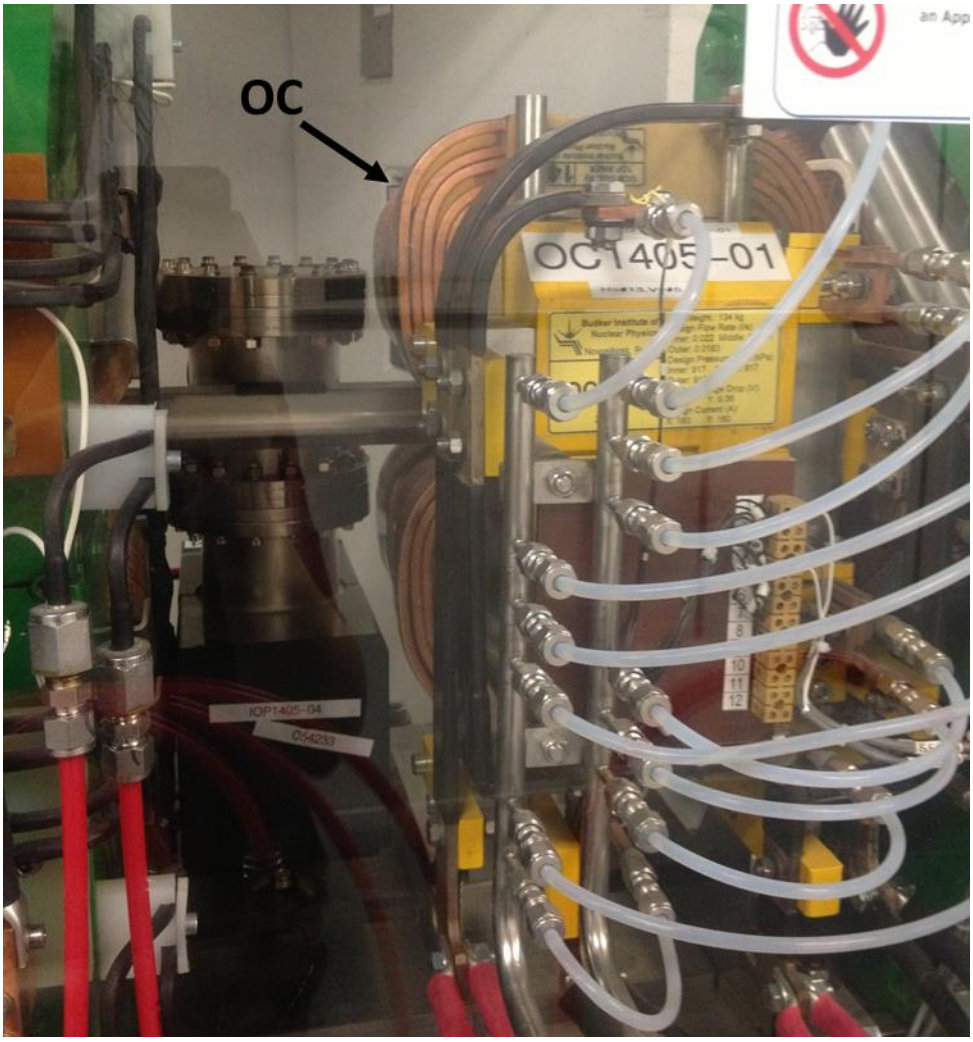

Figure 1- 7 Orbit Corrector (OC). The combined horizontal and vertical orbit corrector used in CLS storage ring. The white translucent tubes carry cooling water for the electromagnets.

There are 48 eBPMs distributed around the ring. The whole ring has 12 cells, in which each cell has 4 eBPMs and 4 vertical orbit correctors (48 in total) for control of the vertical orbit. The horizontal orbit control uses the same four eBPMs and has the same number of correctors (4 correctors per cell × 12 cells = 48 horizontal correctors). Thus there are 96 correctors for the whole ring.

For orbit control the measured electron beam position needs to result in corrector values. Thus, for a given set of 48 values for either horizontal or vertical eBPM values there needs to be

48 currents in the horizontal or vertical OC electromagnets. This transformation between eBPM measurements and OC values results in a 48 by 48 response matrix for horizontal and vertical.

To determine the response matrix, one orbit corrector at a time is energized to deflect the beam by a set angle and then the position of all 48 BPMs is recorded. After all correctors (OC) have been used the result is a 48×48 response matrix. A response matrix (R) is made for both the *x* and *y* directions.

An uncorrected orbit position, P (1×48 vector), measured by the 48 eBPMs can be corrected by inverting the response matrix to calculate the values of all the correctors, OC (1×48 vector), to simultaneously correct the orbit at all eBPMs; i.e.

$$\mathrm{OC} = \mathrm{R}^{-1}\mathrm{P} \qquad (1.3)$$

The zero for the eBPMs is called the "golden orbit" and is made to place the beam in the center of the quads where possible. Beam "bumps" or offsets from the golden orbit can be made by introducing arbitrary offsets at desired locations in P. This feature was used to produce desired position and angle offsets in the BMIT dipole magnet.

1.4 X-RAY DIFFRACTION

X-ray diffraction in crystals arises from constructive interference from reflections from individual lattice planes. Bragg's law describes the relationship between the wavelength of the incident beam, λ, the angle between the incident beam and lattice planes, θ, and the spacing between lattice planes, d (called the d-spacing). Referring to Figure 1- 8, the derivation of Bragg's law involves finding the condition that phase matches specularly reflected waves from lattice planes in the crystal separated by a distance, d.

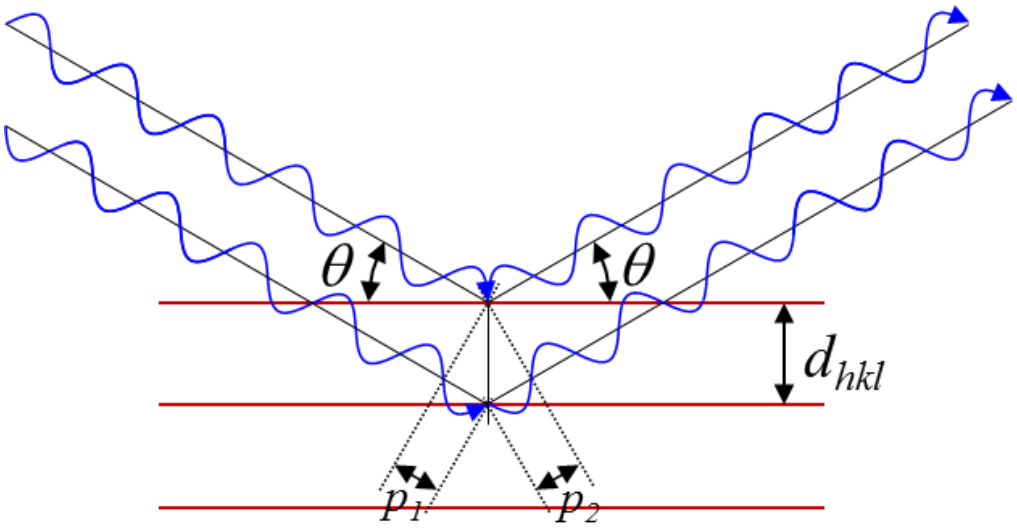

Figure 1- 8 Schematic diagram showing the interference condition for X-rays reflecting from lattice planes that leads to Bragg's law. Figure courtesy Dr. Dean Chapman.

One form of Bragg's law includes the number of wavelength shifts that occur between two subsequent planes as an integer, n. This form is shown in equation (1. 4).

$$n\lambda = 2dsin\theta \tag{1. 4}$$

Commonly, this diffraction order, n, is incorporated into the d-spacing distance in the form of identifying the Miller indices [35], *h, k, l* of the reflection being used. In other words, higher diffraction orders can be thought of as arising from smaller d-spacings as shown in equation (1. 5).

$$\lambda = 2d_{hkl}sin\theta \tag{1. 5}$$

For example of the d-spacing for a cubic type crystal is,

$$d_{hkl} = \frac{a_0}{\sqrt{h^2+k^2+l^2}} \ , \tag{1. 6}$$

where a_0 is the cubic cell dimension.

Silicon is typically used as a monochromator material because it can be crystallized into a perfect lattice. Silicon has a rhombohedral structure, but can be indexed in a cubic system with some restrictions on the *h, k, l* values. Specifically, *h, k* and *l* are all odd such as (1,1,1), (3,1,1)

or all even and the sum of *h, k,* and *l* is 4 times an integer such as (2,2,0), (4,0,0). There are no mixed odd and even *h, k,* and *l* allowed. This is a consequence of indexing the reflections in a cubic system rather than rhombohedral. For silicon the cubic cell dimension is 5.4305 Å.

As mentioned, silicon can be crystallized as a perfect crystal which means that the lattice is un-interrupted over large dimensions of several centimeters to even a sizable fraction of a meter. This amazing feat is a consequence of the drive of the semiconductor industry to make ever better and larger chips for computer and other applications. In terms of x-ray diffraction a perfect crystal has several unique properties that are not typical of crystals found in nature. To describe the perfect crystal's diffraction behavior a dynamical theory is used [36]. This theory self-consistently accounts for the x-ray wavefields interaction with a periodic array of electric dipoles. Most crystals are naturally composed of small, slightly angularly misaligned, crystallites. This then makes large scale interference impossible in such a crystal and a simpler, single interaction diffraction theory can be used, called a kinematic theory.

For our purposes, the one property that is used for monochromators is that a perfect crystal will preserve the beam divergence and phase fronts of the source. At a synchrotron, this property is essential for many research applications. Also, a perfect crystal will have a well-defined reflectivity width (Darwin width [36]) and energy bandwidth over which the crystal will have near unit reflectivity. This effect is shown in Figure 1- 9 which is a graphical view of Bragg's law, but with the magnified inset it can be seen that the plot has an angular width (Darwin width) and a finite vertical size (wavelength range or bandwidth).

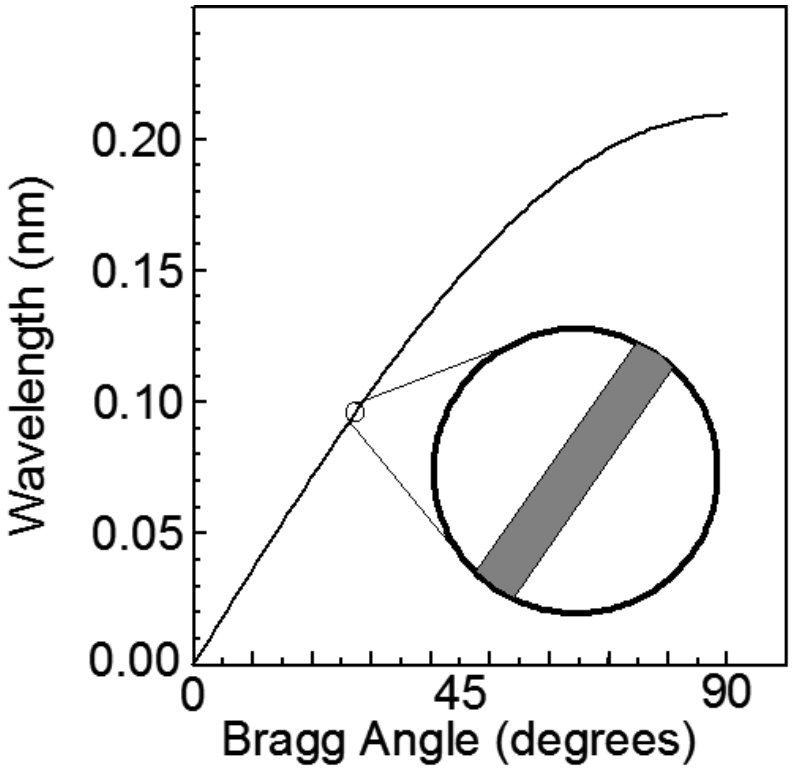

Figure 1- 9 DuMond Diagram. This figure shows the relationship between wavelength and angle to the lattice planes – Bragg's Law – graphically. The magnified insert shows that the curve has a finite angular width (Darwin width) and finite vertical size (bandwidth). Image courtesy Dr. Dean Chapman.

This type of plot showing the wavelength and angle relationship for a crystal is called a DuMond diagram [37]. Usually the wavelength and angle range is limited on the diagram to the region of interest as is shown later on in Figure 1- 12. One interesting aspect of crystals used as monochromators is that they have nearly fixed bandwidths over the usable wavelength or energy range.

1.4.1 Double Crystal Monochromator

A polychromatic beam incident on a crystal will result in diffracted x-ray beams that are somewhat monochromatic according to Bragg's law for the lattice planes in an incident angle to those planes. A single crystal could be used to prepare monochromatic beam for a research application. Tuning the energy of the monochromatic beam will result in that beam moving in

angle and thus the sample as well as other instrumentation required for detection or analysis would need to move to remain fixed in that beam. A method to keep the beam fixed on the sample while tuning the energy is to use a pair of crystals – one to monochromatize the incident beam and one to diffract that beam back parallel to the incident beam. By coordinating the motion of the two crystals, a range of energies can be chosen while keeping the monochromatic beam from the second crystal at the same vertical location [38]. Additionally, if perfect crystals are used, their near unit reflectivity means there is little intensity loss from the pair. This arrangement is commonly called a double crystal monochromator (DCM). The monochromator used on the BMIT-BM beamline operates in pseudo channel cut mode where the two crystals are fixed in relation to each other. As the energy is changed the beam moves vertically but this vertical motion is not noticeable at higher energies (>20 keV) where this monochromator is commonly used; see Figure 1- 10.

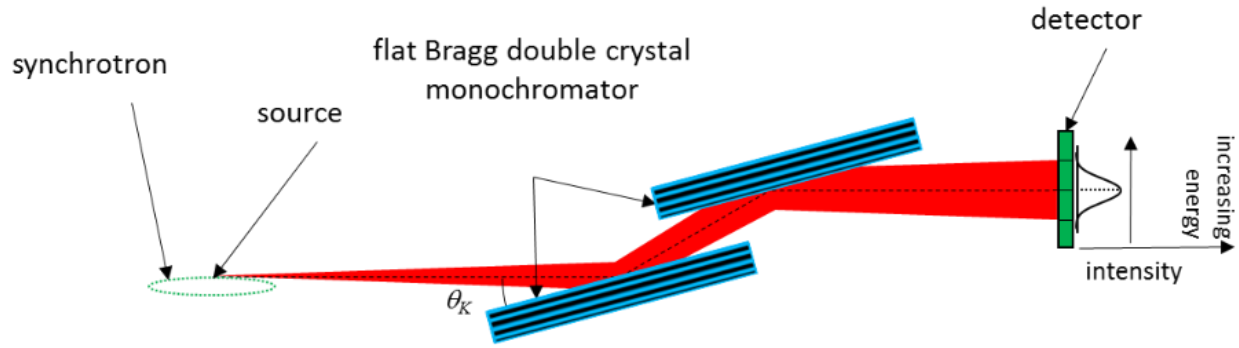

Figure 1- 10 Double Crystal Monochromator (DCM). This type of monochromator is very common on synchrotron beamlines which allows selection of photon energy while keeping the direction and location of the exit monochromatic beam fixed.

1.4.1.1 What happens when the photon beam moves?

The monochromatic beam from a DCM is sensitive to the motion of the photon beam from the source. The two parallel crystals in the DCM behave much like two parallel mirrors with the difference being the angle of incidence of the beam from the source onto the crystals

defines the energy of the output beam. If the source point moves up then the monochromatic beam measured at the detector location will also move up by the same amount. If the beam moves in vertical angle then the monochromatic beam at the detector position will move by the product of the angle times the distance from the source to the detector position. The combination of vertical beam motion and angle is shown below in equation (1. 7);

$$y_d = y + Dy' \ , \tag{1. 7}$$

where y_d is the measured vertical beam position by the imaging detector, y is the vertical position of the electron beam source, y' is the vertical angle of the electron beam source and D is the distance from the source to the detector.

1.5 ABSORPTION EDGES OF ELEMENTS

X-ray absorption edges occur when the x-ray photon has sufficient energy to remove electrons from one of the shells of an atom (photo-electric effect), which results in a dramatic increase in the absorption, directly above this energy. Absorption edge energies are specific to elements, and are strongly dependent to the atomic number of the element (Z). The photo-electric absorption coefficient contribution to the total mass attenuation coefficient, μ/ρ, is Z dependent and E dependent with an approximate Z^3/E^3 type behavior. At higher x-ray energies (i.e. ~30 keV and higher for a low Z material such as water) the Compton effect will be a major contributor to the total attenuation coefficient. This contribution is roughly energy independent and is responsible for the transition from strong energy dependence of water below ~30 kev and relative energy independence above ~30 keV as seen in Figure 1- 11.

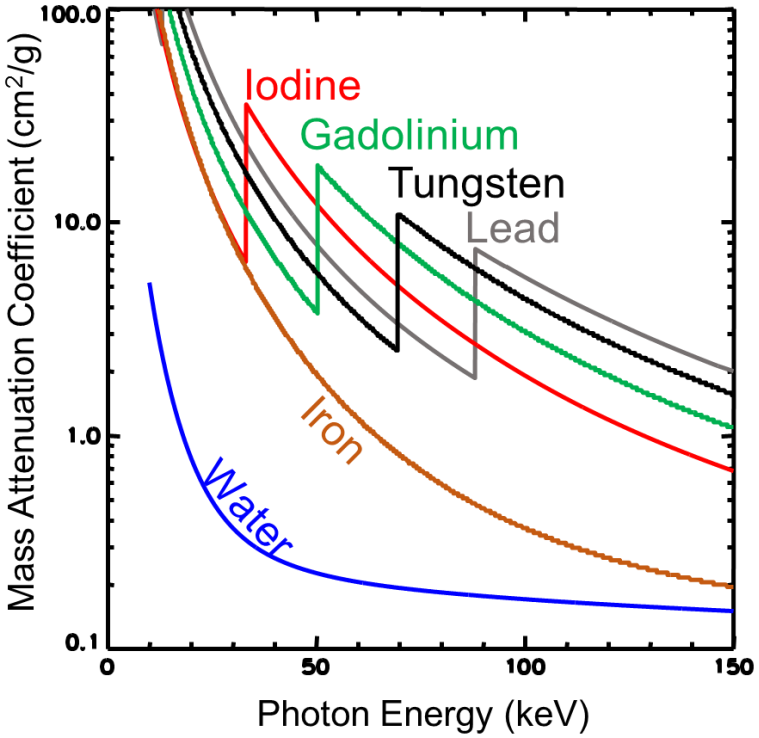

Figure 1- 11 Total Mass Attenuation of selected materials and elements. Data source from reference 39. Image courtesy Dr. Dean Chapman.

Note that all the other example materials have significantly higher Z (Fe : 26, I : 53, Gd : 64, W : 74, Pb : 82) and over the energy range shown, their attenuation is mostly dominated by photo-electric absorption. The mass attenuation coefficient is expressed as a ratio: μ/ρ. This ratio of linear attenuation and mass density is an element or material property which is state independent. For example, the value of μ/ρ of water does not depend on water as a solid, liquid or gas. The product of the μ/ρ with density of the material then gives the linear attenuation coefficient, μ. To calculate the x-ray transmission through a material with density ρ and thickness t, we use the Beer-Lambert law:

$$\frac{I}{I_0} = e^{-\frac{\mu}{\rho}\rho t}, \tag{1. 8}$$

The most tightly bound electrons in an element are in the K (1s) shell. When a DCM is tuned to an absorption edge it is possible to have some of the beam above and some of the beam

below the edge energy, due to dispersion properties of the crystal. This range of energies arises from the fact that angles from the source onto the lattice planes of the crystal result is a range of wavelengths or energies due to the crystals dispersion as shown in Figure 1- 9.

This energy range is easily calculated based on the monochromator reflection used and the angular size of the beam passed through the system.

As an example, assume we use a vertical angle range of $1/\gamma$ = 176 microradians. If we use the Si (2,2,0) reflection in the double crystal monochromator, the d-spacing for this reflection is 0.192 nm. At 33.17 keV (0.03738 nm) the Bragg angle is then 5.586^0. We can calculate the range of wavelengths using the derivative of Bragg's law with respect to angle,

$$\frac{d\lambda}{d\theta} = 2d_{hkl}cos\theta, \tag{1. 9}$$

For the conditions stated the wavelength spread is 6.73×10^{-5} nm centered at 0.03738 nm. The matching energy spread is 59.7 eV

As shown in the DuMond diagrams (Figure 1- 9 and Figure 1- 12), there is also an energy or wavelength spread due to the finite reflectivity width of the dispersion curve. For diffraction, the energy or wavelength bandwidth is a fixed quantity away from absorption edges of the crystal. For Si (2,2,0) the bandwidth is 56.6×10^{-6}. Thus the intrinsic wavelength spread is 2.12×10^{-6} nm and the intrinsic energy spread is 1.88 eV. The energy spread due to divergence is almost 32 times that of the intrinsic energy spread. This range of wavelengths and angles is shown in Figure 1- 12.

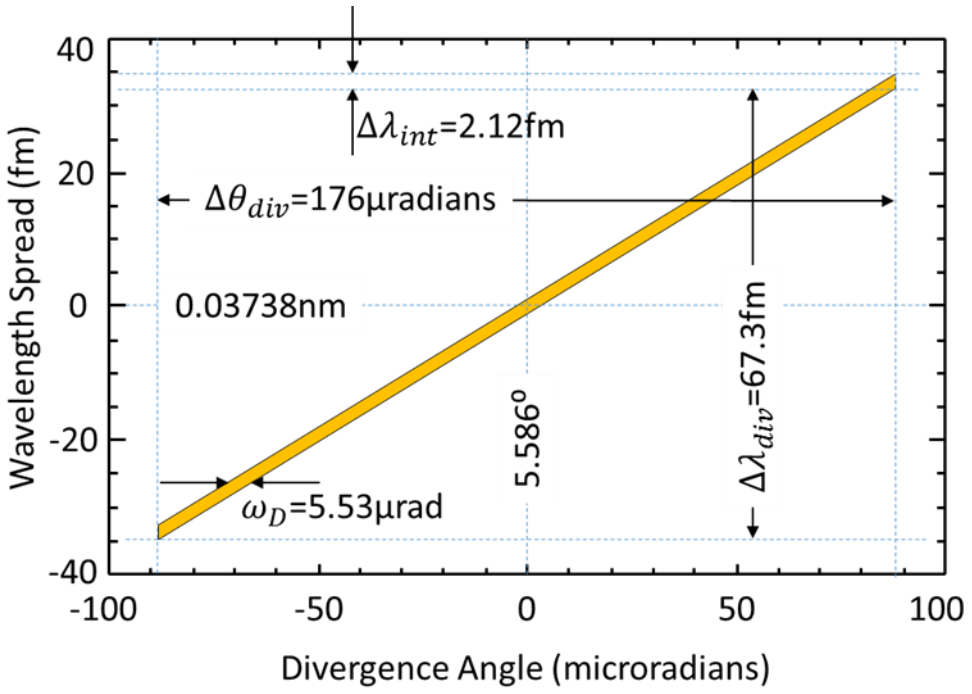

Figure 1- 12 DuMond Diagram for Si (2,2,0) @ 33.17 keV for *1/γ* Vertical Divergence. Additionally, this figure shows the Darwin width, ω_D, which is 5.53 microradians for this energy and reflection.

1.5.1. Double Crystal Monochromator at a K-Edge

Schematically, the effect of an iodine filter on the transmitted beam of a double crystal monochromator set at 33.17 keV is shown in Figure 1- 13.

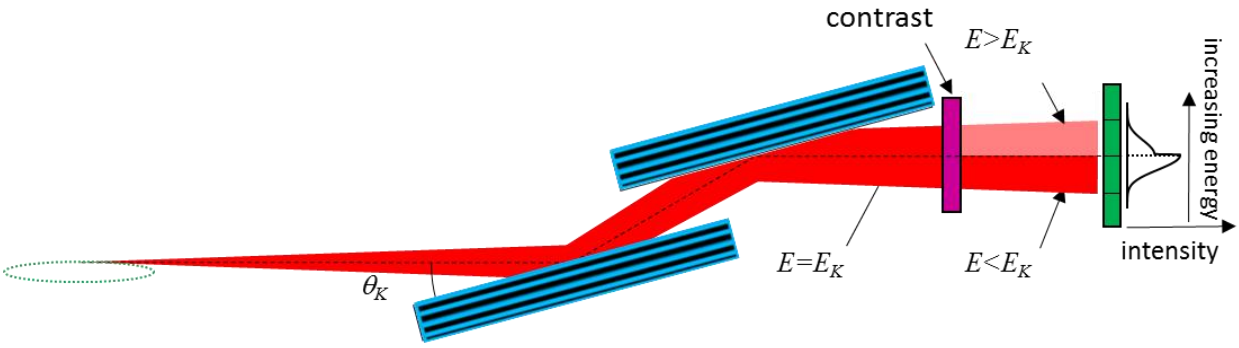

Figure 1- 13 Schematic of double crystal monochromator selecting a median energy at the K-edge of a contrast material. The example plot on the right shows the effect of the K-edge absorption on the transmitted beam.

Note that the spectral content of the beam vertically increases in energy from the bottom of the beam to the top. When the middle energy of that beam is placed at the iodine K-edge then the top of the beam will be absorbed more than the bottom creating an asymmetric beam profile shown on the right side of the figure. A calculation of what this beam shape would be including the DuMond dispersion effects is shown in Figure 1- 14.

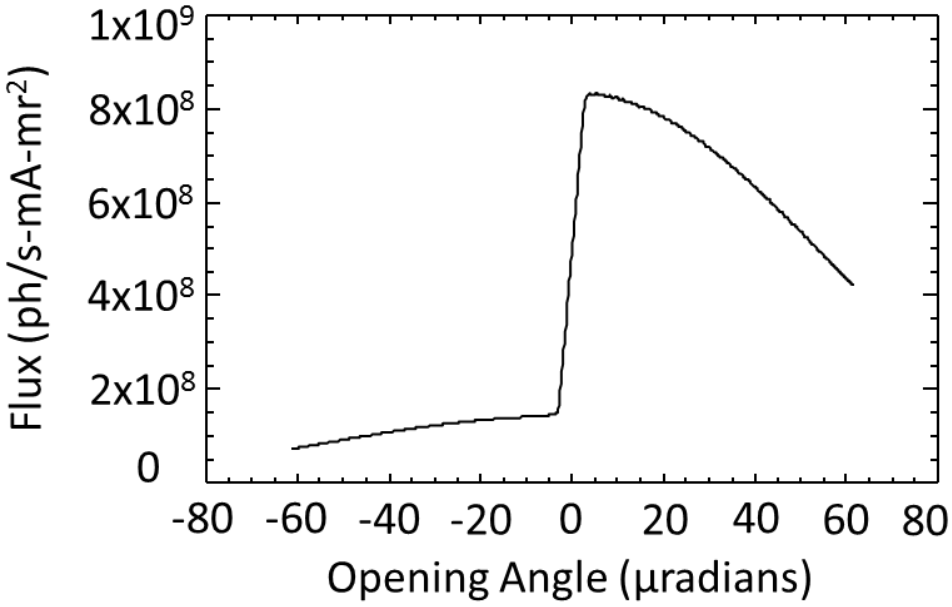

Figure 1- 14 Calculated flux through a 60 mg/cm^2 iodine filter from a Si (2,2,0) DCM at 33.17 keV on a CLS bend magnet beamline.

1.5.1.1 What happens when the beam moves?

When the beam moves at the source in vertical angle or position, the beam filtered by the K-edge material behaves differently than the case discussed above. The K-edge is a fixed energy and will find the location of that energy in the beam. If the source moves vertically the location of the K-edge will move the same amount at the detector location. If instead the beam at the source moves in vertical angle the location of the edge will not move. Therefore the location of

the edge is a direct measure of the location of the source vertically. The location of the edge measured at the detector position is then,

$$y_c = y, \tag{1. 10}$$

where y_c is the measured vertical K-edge position and y is the vertical position of the electron beam source.

1.6 REFERENCES

1. Nolte, D.D., The tangled tale of phase space. Physics Today, 2010. 63(4): p. 33-38.
2. Brefeld W. Stabilization of synchrotron radiation beam at HASYLAB (invited). Review of Scientific Instruments. 1989;60(7):1513-6.
3. Galimberti A, Borghes R. Operational Experience with the Photon Beam Position Monitor for Undulator Beamlines of Elettra. AIP Conference Proceedings. 2004;705(1):584-7.
4. K. Haga, M. Nakayama, K. Masuda, H. Ishizaki, M. Kura, L. Meng, et al., editors. The Vibration Measurements at the Photon Factory Storage Ring Building. European Particle Accelerator Conference; 2000; Vienna, Austria.
5. Rehm G. Achieving and Measuring Sub-Micrometer Beam Stability at 3rd Generation Light Sources. Journal of Physics: Conference Series. 2013;425:042001.
6. Bocchetta CJ, editor Lifetime and beam quality. CAS - CERN Accelerator School 1996; Grenoble, France. Geneva1997.
7. Farvacque L, editor Beam Stability. CAS - CERN Accelerator School; 1996; Grenoble, France. Geneva1997.
8. Hettel R. Review of synchrotron beam stability and stabilizing systems (invited). Review of Scientific Instruments. 1989;60(7):1501-6.
9. Hettel RO. Beam stability at light sources (invited). Review of Scientific Instruments. 2002;73(3):1396-401.
10. Alkire RW, Rosenbaum G, Evans G. Design of a vacuum-compatible high-precision monochromatic beam-position monitor for use with synchrotron radiation from 5 to 25 keV. Journal of Synchrotron Radiation. 2000;7(2):61-8.
11. Bergonzo P, Tromson D, Mer C. CVD diamond-based semi-transparent beam-position monitors for synchrotron beamlines: preliminary studies and device developments at CEA/Saclay. Journal of Synchrotron Radiation. 2006;13(2):151-8.
12. Billing MG. Beam position monitors for storage rings. Nuclear Instruments and Methods in Physics Research Section A: Accelerators, Spectrometers, Detectors and Associated Equipment. 1988;266(1–3):144-54.
13. Bunk O, Pfeiffer F, Stampanoni M, Patterson BD, Schulze-Briese C, David C. X-ray beam-position monitoring in the sub-micrometre and sub-second regime. Journal of Synchrotron Radiation. 2005;12(6):795-9.
14. Cheng XC, Zhao FY, Tian YC, Xu CY. V-coupling-blades beam position monitor for NSRL undulator source. Journal of Physics: Conference Series. 2013;425.
15. Ilinski P, Hahn U, Schulte-Schrepping H, Degenhardt M. Residual Gas X-ray Beam Position Monitor Development for PETRA III. AIP Conference Proceedings. 2007;879(1):782-5.

16. Izumi T, Nakajima T, Kurihama T. Photon beam position monitor. Review of Scientific Instruments. 1989;60(7):1951-2.

17. Johnson ED, Oversluizen T. Compact high flux photon beam position monitor. Review of Scientific Instruments. 1989;60(7):1947-50.

18. Kyele NR, Decanniere K, van Silfhout RG. A transparent two-dimensional in situ beam-position and profile monitor for synchrotron X-ray beamlines. Journal of Synchrotron Radiation. 2005;12(6):800-6.

19. Leban P, Tinta D, Pradervand C, editors. Photon Beam Position Measurements using CVD Diamond based Beam Position Sensor and Libera Photon at Swiss Light Source. International Particle Accelerator Conference; 2010; Kyoto, Japan.

20. Muller EM, Smedley J, Bohon J, Yang X, Gaowei M, Skinner J, et al. Transmission-mode diamond white-beam position monitor at NSLS. Journal of Synchrotron Radiation. 2012;19(3):381-7.

21. Revesz P, Temnykh AB, Pauling AK. New X-ray beam position monitors with submicron resolution utilizing imaging of scattered X-rays at CHESS. Nuclear Instruments and Methods in Physics Research Section A: Accelerators, Spectrometers, Detectors and Associated Equipment. 2011;649(1):94-6.

22. Tucoulou R, Martinez-Criado G, Bleuet P, Kieffer I, Cloetens P, Labouré S, et al. High-resolution angular beam stability monitoring at a nanofocusing beamline. Journal of Synchrotron Radiation. 2008;15(4):392-8.

23. van R. A high-precision X-ray beam-position and profile monitor for synchrotron beamlines. Journal of Synchrotron Radiation. 1999;6(6):1071-5.

24. Xiao Y, Sun B, Gu L, Lu P, Wang J, Tang L, et al. Development of a PSD-based photon beam position measurement system. Nuclear Science and Techniques. 2012;23:70-4.

25. Kachatkou A, Kyele N, Scott P, van Silfhout R. In situ X-ray beam imaging using an off-axis magnifying coded aperture camera system. Journal of Synchrotron Radiation. 2013;20(4):596-602.

26. Hahn U, Brefeld W, Hesse M, Schneider JR, Schulte-Schrepping H, Seebach M, et al. Beam-position monitors in the X-ray undulator beamline at PETRA. Journal of Synchrotron Radiation. 1998;5(3):627-9.

27. Kyele NR, van Silfhout RG, Manolopoulos S, Nikitenko S. In situ synchrotron x-ray photon beam characterization. Journal of Applied Physics. 2007;101(6):064901.

28. Morse J, Solar B, Graafsma H. Diamond X-ray beam-position monitoring using signal readout at the synchrotron radiofrequency. Journal of Synchrotron Radiation. 2010;17(4):456-64.

29. Bergstrom JC, Vogt JM. The optical diagnostic beamline at the Canadian Light Source. Nuclear Instruments and Methods in Physics Research Section A: Accelerators, Spectrometers, Detectors and Associated Equipment. 2006;562(1):495-512.

30. Wysokinski TW, Chapman D, Adams G, Renier M, Suortti P, Thomlinson W. Beamlines of the biomedical imaging and therapy facility at the Canadian light source—Part 1. Nuclear Instruments and Methods in Physics Research Section A: Accelerators, Spectrometers, Detectors and Associated Equipment. 2007;582(1):73-6.

31. Wysokinski TW, Chapman D, Adams G, Renier M, Suortti P, Thomlinson W. Beamlines of the Biomedical Imaging and Therapy Facility at the Canadian Light Source - Part 2. Journal of Physics: Conference Series. 2013;425 Part 7.

32. Zhu Y, Samadi N, Martinson M, Bassey B, Wei Z, Belev G, et al. Spectral K-edge subtraction imaging. Physics in Medicine and Biology. 2014;59(10):2485-503.

33. Thompson A. X-Ray Data Booklet. In: Energy Do, editor. rev 3 ed. Berkeley, CA USA: Lawrence Berkely Laboratory; 2009.

34. Bertwistle D. CLS Button Position Monitor Sensitivity Analysis. 2001-11-14.

35. Warren BE. X-Ray Diffraction: Dover Publications; 2012.

36. Als-Nielsen J, McMorrow D. Elements of Modern X-ray Physics: Wiley; 2011.

37. DuMond JWM. Successive x-ray crystal reflections to obtain increased resolving power. Physical Review. 1937;52:872-83.

38. Golovchenko JA, Levesque RA, Cowan PL. X-ray monochromator system for use with synchrotron radiation sources. Review of Scientific Instruments. 1981;52(4):509-16.

39. Lighthill, F.B.a.R., Analytical Approximations for X-Ray Cross Sections III, S.N. Laboratories, Editor. 1988: Albuquerque, NM

CHAPTER 2

This paper was published in the Journal of Synchrotron Radiation in April 2015 (Samadi, N., et al., A phase-space beam position monitor for synchrotron radiation. J Synchrotron Radiat, 2015. 22(4): p. 946-55). I took all of the data and did all of the data analysis. I arranged for the beamtime and coordinated data acquisition with the beam motion studies. Others were involved in the experimental setup (Martinson, Belev), literature search (Bassey), storage ring properties and predicted beam motions (Dallin, de Jong) and algorithm development (Chapman). I and Prof. Chapman prepared the manuscript draft which was reviewed by the other co-others.

A PHASE SPACE BEAM POSITION MONITOR FOR SYNCHROTRON RADIATION

Nazanin Samadi[a]*, Bassey Bassey[b], Mercedes Martinson[b], George Belev[c], Les Dallin[c], Mark de Jong[c], Dean Chapman[d]

[a]Biomedical Engineering, University of Saskatchewan, 107 Wiggins Rd, Saskatoon, SK, S7N 5E5 Canada

[b]Physics and Engineering physics, University of Saskatchewan, 116 Science Place, Saskatoon, SK, S7N 5E2 Canada

[c]Canadian Light Source, 44 Innovation Boulevard, Saskatoon, SK, S7N 2V3, Canada

[d]Anatomy and Cell Biology, University of Saskatchewan, 107 Wiggins Rd, Saskatoon, SK, S7N 5E5, Canada

Correspondence email: nazanin.samadi@usask.ca

Keywords: beam position monitor, x-ray diffraction, k-edge absorption, phase space

Synopsis A system has been developed to measure the vertical position and angle of the electron beam at a single location from a synchrotron source. The system uses a monochromator tuned to the absorption edge of a contrast material and has a sensitivity comparable to other beam position monitors

2.1 ABSTRACT

The stability of the photon beam position on synchrotron beamlines is critical for most if not all synchrotron radiation experiments. The position of the beam at the experiment or optical element location is set by the position and angle of the electron beam source as it traverses the magnetic field of the bend magnet or insertion device. Thus an ideal photon beam monitor would be able to simultaneously measure the photon beam's position and angle, and thus infer the electron beam's position in phase space.

X-ray diffraction is commonly used to prepare monochromatic beams on x-ray beamlines usually in the form of a double crystal monochromator. Diffraction couples the photon wavelength or energy to the incident angle on the lattice planes within the crystal. The beam from such a monochromator will contain a spread of energies due to the vertical divergence of the photon beam from the source. This range of energies can easily cover the absorption edge of a filter element such as iodine at 33.17 keV. A vertical profile measurement with and without the filter can be used to determine the vertical angle and position of the photon beam. In these measurements an imaging detector measures these vertical profiles with an iodine filter that horizontally covers part of the monochromatic beam.

The goal was to investigate the use of this combined monochromator, filter and detector as a phase space beam position monitor. The system was tested for sensitivity to position and angle under a number of synchrotron operating conditions, such as normal operations and special operating modes where the beam is intentionally altered in position and angle. The results are comparable to other methods of beam position measurements and indicate that such a system is feasible in situations where part of the white synchrotron beam can be used for the phase space measurement.

2.2 INTRODUCTION

The trajectory of a photon beam can be determined if both the position and angle can be found at some point along the propagation direction. From knowledge of this beam's position and angle or its position in phase space, it is possible to transform back to the source and determine the source coordinates in phase space if the optics in the intervening locations and their effects are known.

This paper describes a method to simultaneously measure the photon beam position and angle at one location. This system was developed at the Canadian Light Source (CLS) on the Biomedical Imaging and Therapy (BMIT) bend magnet beamline 05B1-1 (BM).

The CLS is a third generation synchrotron facility with a low electron beam emittance (ε_x = 18 nm-rad, ε_y = 0.10 nm-rad). Beam instability, be it electron or photon beam, can be a concern especially to the third generation facilities. It has adverse effects on the required low electron beam emittance, effective brilliance of the synchrotron radiation, and experiments performed at the experimental stations [1-4]. The causes of beam instability and the methods of reduction have been widely studied [5-8], and the drive to ensure and maintain a steady beam has led to the development of different types of beam monitors [9-23].

Photon beam position and angle instabilities at experimental stations are attributed to fluctuations of stored electron beam orbit and vibrational and thermal distortion of beamline optical components. The usual target for stability in the vertical plane is 10 % of the beam size in position and angle [8]. Most of the available photon beam monitors are sensitive to the beam position only, and hence the name photon beam-position monitors (PBPM). However, the measured beam position is determined by both the source position and angle. A single PBPM does not provide independent information about the photon beam source position and angle [18,

24]. The photon beam angle needs to be monitored to account for the negative effects of beam angle instability [18, 25-27]. The use of two photon PBPMs is common, when the position and angle of a photon beam is to be measured [18, 22, 23].

At the CLS, beam instabilities are monitored by two diagnostic beamlines - the Optical Synchrotron Radiation (OSR) and the X-ray Synchrotron Radiation (XSR) beamlines [28]. Most beamlines at the CLS have provision for some type of PBPMs, but few are actually implemented or used. These monitors are of the type that measure only the photon beam position at some location in the beamline.

As with almost all synchrotron experiments imaging is affected by photon beam motion. One of the imaging methods used at BMIT beamline is K-edge subtraction using an iodine contrast element with a beam prepared by a bent Laue monochromator. Measurements made with this system during a period of electron beam instability gave the idea that we can measure the photon beam position and angle or from it infer the electron beam's position in phase space.

We present a method for measuring the position and angle of a photon beam simultaneously – a phase space – Beam Position Monitor (ps-BPM). The method relies on the energy dispersive properties of flat crystals and makes use of the absorption edge of a filter in the photon beam path to determine a specific energy or angle of the photon beam. This, coupled with a measurement of the beam in the absence of the filter, allows beam position and angle to be determined.

2.2.1 Synchrotron Radiation

The single electron vertical photon emission distribution is properly described by a modified Bessel function of the second kind [29]; however, this distribution is well modelled as a Gaussian function. This vertical angular distribution mostly falls within a $1/\gamma$ range in the X-ray

where γ is the electron beam energy divided by the electron rest mass (γ=5675 for the CLS). The electron beam size and vertical angle distribution can also be described as a Gaussian function. Therefore, the bend magnet synchrotron beam has a vertical distribution that is nearly Gaussian. A measured comparison of the vertical distribution of the beam on the CLS BMIT bend magnet beamline is shown in Figure 1- 3 at 33.17 keV. As measured some distance from the source, the vertical angle or position motion of the electron source will move this distribution vertically. Because the measurement distance from source can be tens of meters, the angle affects are amplified. For example, the profile measured in Figure 1- 3 is at 26 m from the electron beam source. In this figure the blue line is the measured profile from the image at the top of the figure. The red dashed line is a Gaussian fit to that profile.

The fact that the red dashed line is hard to see indicates how closely the Gaussian fit is to the actual beam profile. The black dashed line is a calculated profile from the modified Bessel function [29] for the actual conditions of the measurement [CLS Bend Magnet (2.9 GeV & 1.354 T) at 26 m from the source with 100 μm pixels and 33.17 keV photon energy].

2.2.2 Double Crystal Monochromator at an Absorption Edge

Diffraction of x-rays in crystals can be thought of as arising from constructive interference from reflections at lattice planes as described by Bragg's law,

$$\lambda = 2d_{hkl}sin\theta, \qquad (2.\ 1)$$

where λ is the wavelength of the diffracted beam, θ is the angle between the incident beam and lattice planes, d_{hkl} (called the d-spacing) is the spacing between the (h,k,l) lattice planes.

For an x-ray synchrotron beamline, usually a pair of parallel crystals is used – one to monochromatize the incident beam and one to diffract that beam back parallel to the incident beam. With a coordinated motion of the two crystals, a range of energies can be chosen while

keeping the monochromatic beam from the second crystal in the same location which is very useful for much of the research being done. Additionally, the near unit reflectivity of the perfect crystals often used means there is little intensity loss from the pair. This arrangement is commonly called a double crystal monochromator (DCM) [30].

When a DCM is tuned to an energy some of the beam will be above and some below the mean energy , for example, the K- edge energy of an element, some of the transmitted beam will be above and some below the mean energy due to the dispersion properties of the crystals. This range of energies arises from the range of incident photon beam angles onto the lattice planes of the crystal and/or the energy bandwidth of the crystal and the reflection used. The range of energies due to angular divergence onto the planes is easily calculated using Bragg's law based on the monochromator reflection used and the angular size of the beam passed through the system. A schematic of a DCM arrangement is shown in Figure 2- 1.

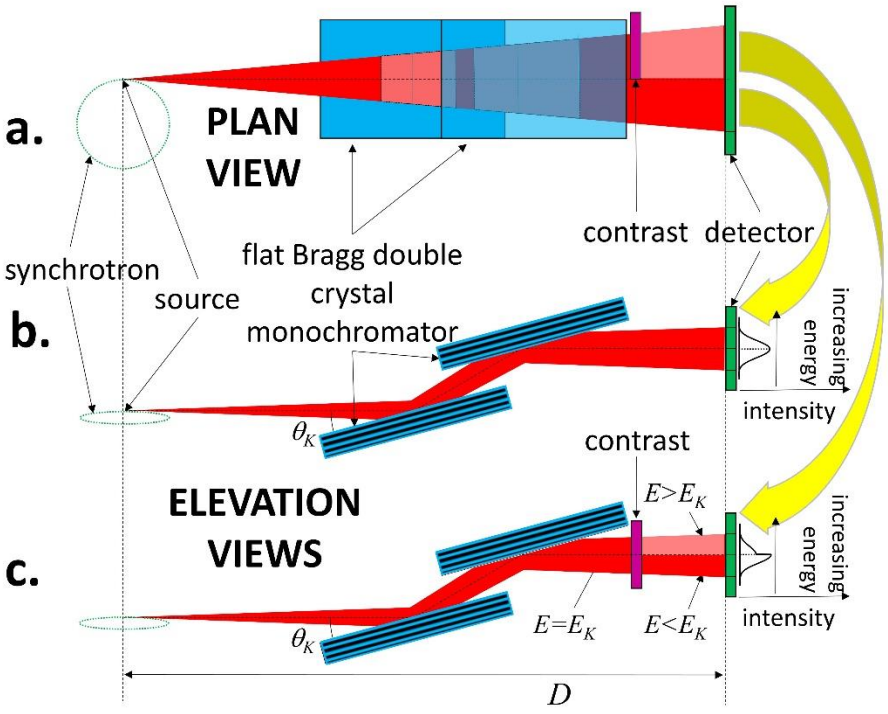

Figure 2- 1 Schematic of the system used at BMIT bend magnet beamline. (a) Plan view of the double crystal monochromator (DCM), contrast material and detector. (b) Elevation view of the

non-contrast or beam side; (c) elevation view with contrast material whose K-edge is at the vertical middle beam prepared by the DCM. Example plots at the right show the profile for the unfiltered beam (b) and contrast filtered beam (c).

As an example, assume a vertical angle range for the CLS of $1/\gamma = 176$ μrad. At 33.17 keV, the absorption edge of iodine, the Bragg angle is 5.586^0 for the silicon (2, 2, 0). We can estimate the range of wavelengths using the derivative of Bragg's law with respect to angle,

$$d\lambda = 2d_{hkl}cos\theta d\theta. \qquad (2.\ 2)$$

For the conditions stated the wavelength spread is 6.73×10^{-5} nm centered at 0.03738 nm. The matching energy spread is 59.7 eV. Figure 2- 2 is a graphical representation, a DuMond diagram [31], of Bragg's law in the vicinity of the iodine K-edge.

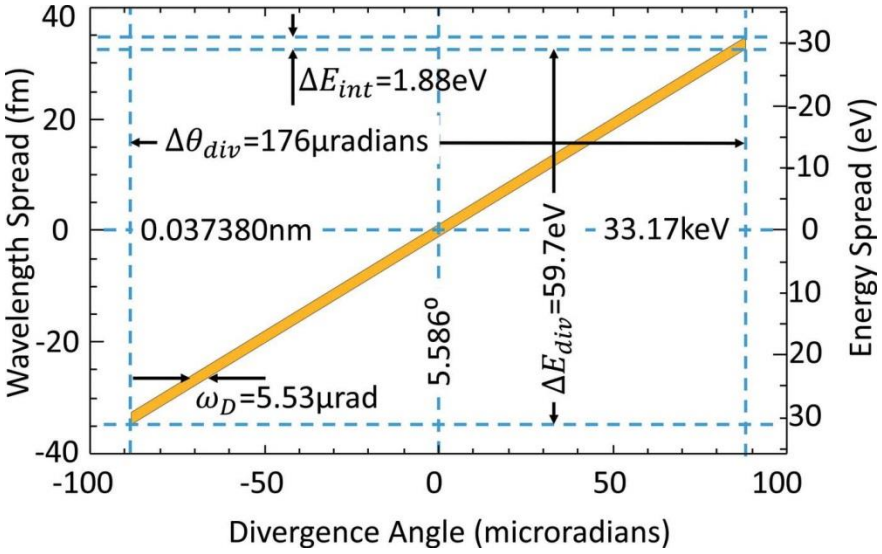

Figure 2- 2 DuMond Diagram for Si (2,2,0) at 33.17 keV for $1/\gamma$ vertical divergence. The energy and angular ranges are shown for both vertical divergence and intrinsic widths. The relatively large vertical divergence results in an energy range that easily covers the K-edge of iodine.

There is also an energy or wavelength spread due to the finite reflectivity width of the dispersion curve. For diffraction, the energy or wavelength bandwidth is a fixed quantity away from absorption edges of the crystal. For silicon (2,2,0) the bandwidth is 56.6×10^{-6}. Thus the intrinsic wavelength spread is 2.12×10^{-6} nm and the intrinsic energy spread is 1.88 eV. This

wavelength and energy spread is also shown in Figure 2- 2. The energy spread due to divergence is almost 32 times that of the intrinsic energy spread.

Schematically, the effect of an iodine filter on the transmitted beam of a DCM set at 33.17 keV is shown in Figure 2- 1(c). Note that the spectral content of the beam vertically increases in energy from the bottom of the beam to the top. When the middle energy of that beam is placed at the iodine K-edge then the top of the beam will be absorbed more than the bottom creating an asymmetric beam profile shown on the right side of the figure. A calculation of the beam shape including the DuMond dispersion effects is shown in Figure 2- 3.

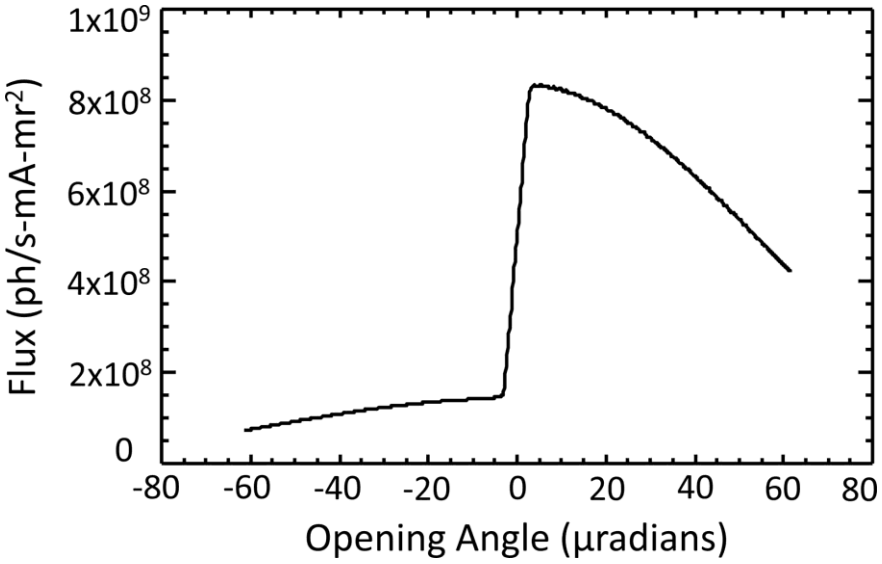

Figure 2- 3 Calculated flux through a 60 mg cm^2 iodine filter from a Si (2, 2, 0) DCM at 33.17 keV on a CLS bend-magnet beamline.

2.3 WHAT HAPPENS WHEN THE BEAM MOVES?

2.3.1 Unfiltered side of the beam

When the photon beam moves at the source location the monochromatic beam after the DCM is sensitive to the motion. If the source point moves up then the beam measured at the detector location will also move up by the same amount. If the beam moves in vertical angle then the beam at the detector position will move by the product of the angle times the distance

from the source to the detector. This effect is shown schematically in Figure 2- 4(a) - Figure 2-4(d) in the 'Beam' column. The combination of vertical beam motion and angle is shown below in equation (2. 3);

$$y_d = y + Dy', \tag{2. 3}$$

where y_d is the measured vertical beam position at the imaging detector, y is the vertical position of the electron beam source, y' is the vertical angle of the electron beam source and D is the distance from the source to the detector.

2.3.2 K-edge filtered side of the beam

The K-edge of an element is a fixed energy and can be used to locate of that energy in the photon beam; energies above the edge will be heavily absorbed and energies below the edge will not. If the source moves vertically the location of the K-edge will move the same amount at the detector. This is because the vertical energy distribution of the photon beam is not altered by this motion. If instead the beam at the source moves in vertical angle the location of the edge will not move. In this case the vertical photon beam distribution is changed by the DCM but the vertical location of the K-edge at the detector will not move because the angle is set by the monochromator. Therefore the location of the K-edge is a direct measure of the location of the source vertically. This effect is shown schematically in Figure 2- 4(a) - Figure 2- 4(d) in the "Edge" column. The location of the edge measured at the detector is then simply

$$y_c = y, \tag{2. 4}$$

where y_c is the measured vertical K-edge location and y is the vertical position of the electron beam source. Changes in the vertical source angle do not change the location of the K-edge at the detector.

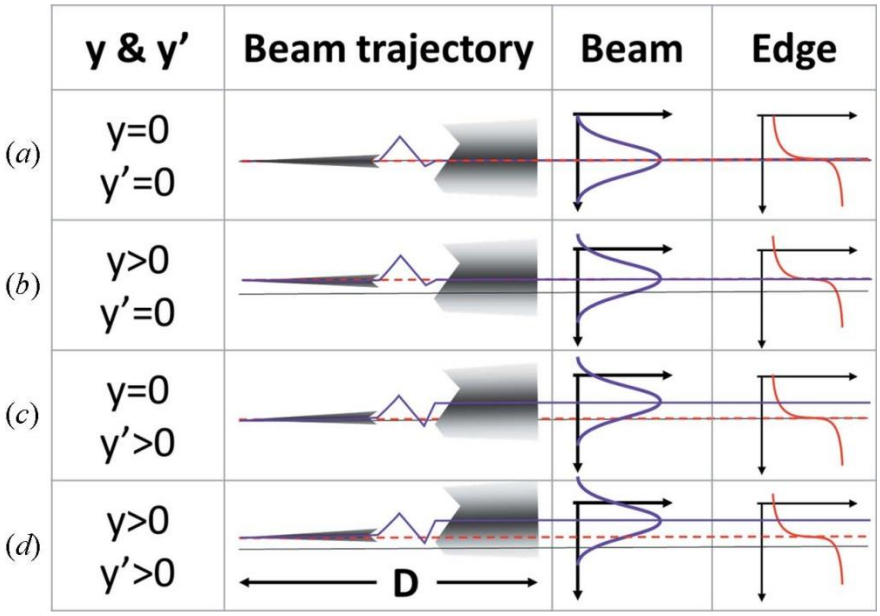

Figure 2- 4 Schematic showing the effects of the electron beam position and angle displacements. The first column gives the position and angle, the second column is a schematic of the beam where the monochromator has been removed for clarity, the third and fourth columns show the beam and edge profile, respectively. The black line in each row represents the electron beam position and angle zeros, the purple line shows the centroid of the beam, the red dashed line shows the location of the same angle to the monochromator crystal or the edge location. (a, c) At $y = 0$. (a, b) At $y' = 0$. (b, d) At $y > 0$. (c, d) At $y' > 0$.

2.4 DETERMINING THE ELECTRON SOURCE VERTICAL POSITION AND ANGLE

We are now in a situation to be able to independently determine the vertical electron beam position and angle by measuring the beam location through a DCM without a filter (beam side) and the edge location with a K-edge filter in place (edge side). Using the equations (2. 3) and (2. 4),

$$y = y_c \quad \& \quad y' = \frac{y_d - y_c}{D} \tag{2. 5}$$

It should be noted that changing the monochromator energy has the effect of changing the source position, y_c. Also changing the detector's vertical position will alter the y_d value. Both have a direct impact on the calculated electron beam position and angle, y and y'. Thus the

system measures relative values of position and angle and must be calibrated to obtain absolute values.

The ability to determine the location of the beam centroid, y_d, and the K-edge, y_c, are integral to the success of this method. A fitting procedure will be used to determine the location of each. To be properly fit there needs to be sufficient intensity, detector resolution and vertical size to encompass the profile along with any vertical motion that may occur. The vertical beam size at the detector is a relatively weak function of the energy selected by the monochromator. However, the reflection chosen in the monochromator may have a strong effect on the intensity since the reflection sets the monochromator bandwidth.

In addition, the ability to determine y_c will also depend on the width of the K-edge and the thickness and density of the contrast filter. A rough estimate of the optimal projected iodine filter density was found to be ~70 mg/cm^2 by numerical simulation. This estimate was based on a contrast to noise model using Poisson statistics.

The width of the transmitted K-edge with the DCM will depend on the intrinsic K-edge width for the contrast element (~15 eV for iodine [32]). The K-edge will also be blurred by the intrinsic energy width of the monochromator (1.88 eV as discussed above for the Si (2,2,0) at 33.17 keV), and will also be dispersed vertically, z, across the detector approximately as,

$$\frac{dz}{dE} = \frac{tan\theta}{E} D, \tag{2. 6}$$

where θ is the Bragg angle and E is the K-edge energy. For the silicon (2,2,0) at the iodine K-edge this spatial dispersion is 74 μm eV^{-1}. Therefore, the 15 eV of energy spread will correspond to a spatial width of 1.1 mm.

When compared with the silicon (4,4,0) under similar conditions the spatial dispersion at 33.17 keV will change to 150 μm eV^{-1} and the 15 eV energy spread will correspond to a width of

~2.2 mm which indicates the increased spatial dispersion sensitivity. But this sensitivity will come with a loss of intensity of over a factor of six due to the decreased (4,4,0) bandwidth (9.1×10^{-6}) compared with the (2,2,0) bandwidth (56.6×10^{-6}) and therefore, for the of the measurements, we chose silicon (2,2,0) .

2.5 IMPLEMENTATION AT BMIT

The experiments for this project where performed at the CLS BMIT bend magnet beamline 05B1-1. A silicon (2,2,0) and (4,4,0) double crystal monochromator was tuned to the iodine K-edge at 33.17 keV. The vertical dispersion of the monochromator allows an energy range that covers the K-edge of iodine. Figure 2- 4(a) - Figure 2- 4Figure 2- 4(c) show schematically how the system was implemented in the beamline with a plan view at the top. In this system the beam was split horizontally in two parts: one side with 60 mg cm^{-2} iodine filter and the other side with no filter. A Hamamatsu flat-panel detector with 0.1 mm pixel size was used to collect data. Measurements were made in the POE-2 hutch, which was ~25 m away from the source.

Two types of measurements were performed. One type was made during the normal operational mode to assess the beam stability. A second type was made during special shifts were the synchrotron beam was intentionally moved at the source location with specific vertical, horizontal and angular offsets. This second type was used to assess, in part, the sensitivity of the system and to independently measure the motions made to the electron beam source in the ring.

Data were in the form of images of the split beam with the iodine filter on one side and no filter on the other. Sets of 400 data images were saved into individual directories and a measurement set might range from a few to several hundred directories. It took around 12 s to collect 400 images for each directory and roughly 1 min dead-time to save the data to the disk.

For each set of measurements, ten dark images (the detector response without beam) and ten flat images (no contrast agent in the beam) were also collected for data normalization. These ten images were averaged to form single 'dark' and 'flat' images.

2.6 DATA ANALYSIS METHOD

To analyze the data, several procedures were written in IDL [Interactive Data Language, ITT Visual Information Solutions, Boulder, CO, USA]. Regions for the unfiltered beam side and the K-edge side were selected from the data and each side was corrected for dark response. An example of the regions chosen from the images is shown in Figure 2- 5.

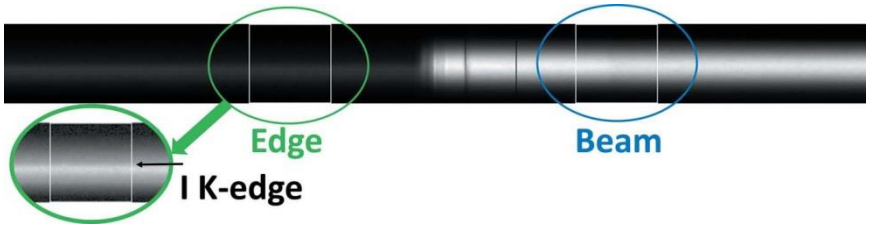

Figure 2- 5 Example data image. Regions are chosen from both image types for beam and edge analysis. The edge region is enhanced in the lower left corner to better show the K-edge whose location is indicated by the arrow.

The beam side from the data was used to determine y_d which was found by fitting the horizontally averaged vertical beam profile using a Gaussian function. An example of this fitting was shown in Figure 1- 3. The vertical direction in the detector, z, was measured in terms of detector pixels that can be easily converted into micrometers using the pixel size. The vertical center of the detector was the origin used in this part of the analysis.

The horizontally averaged edge side profile was normalized by the matching region from the flat to form an I/I_0 profile. However, the flat was corrected for vertical beam motion by using the beam side of the data to vertically move the flat prior to normalization. The low-intensity

regions of this corrected flat were ignored using a threshold value and not used in the analysis. An example of this is shown in Figure 2- 6.

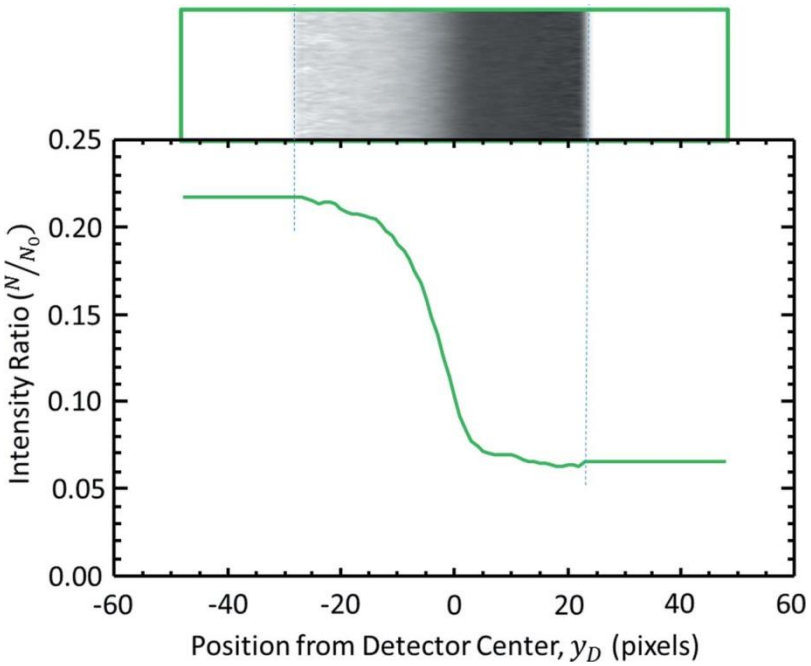

Figure 2- 6 Summed normalized K-edge image across the sampling width; 100 pixels in this case. The horizontal axis is in pixels and the origin is referenced to the vertical middle of the detector.

A number of fitting algorithms were used to find the location of the K-edge in the filtered beam profile. In general, three types of functions were investigated to fit the edge: Gaussian, Lorentzian and Voigt. These functions were chosen because they are mathematically simple and make physical sense. The functions were used directly to fit the derivative of the K-edge profile, and integrated versions of each were used to fit the measured edge profile directly. Finally the K-edge could be fit to the I/I_0 values or the negative logarithm of the I/I_0 values. Of the 12 fit types the Gaussian fit to the derivative of the negative logarithm of the profile was chosen due to its simplicity and the robustness of the fit. For this analysis the main parameter of interest in the fit was the transition center location. Other parameters determined in the fit were the amplitude, width and the background values. Figure 2- 7 shows a fit to one of the data points.

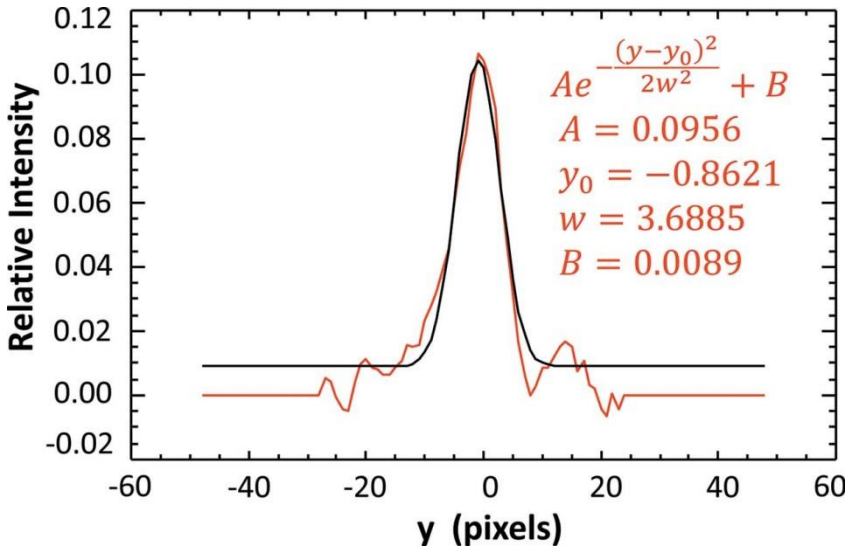

Figure 2- 7 Derivative of the negative logarithm of the profile shown in Figure 2- 6. The Gaussian fit parameters are shown in the upper right-hand corner. For this analysis only y_0 or the peak center is used.

2.7 RESULTS AND DISCUSSION

A number of measurements have been taken with the system. In total, eight shifts (1 shift = 8 h) have been used for beam motion measurements. These shifts were during normal operations shifts and by special request shifts when the ring parameters can be altered. During the special machine study shifts the electron beam was moved and measurements were made to assess the response of the system.

2.7.1 System Response to Electron Beam Motions

The electron beam position and angle were varied in the machine study shifts. To move the electron beam in the BMIT sector, electron BPM (eBPM) target values were changed. This change in target value moves the electron beam orbit using dipole steering magnets. The eBPMs numbered 17 and 18 are located on the upstream and downstream sides of the bend magnet which is our photon beam source (see figure 2- 8). The photon beam source is 5° into 15° bend. Since we observe the photon beam source point at an intermediate location between the two

eBPMs, there can be small differences in the electron beam vertical position and angle due to the storage ring magnetic optics.

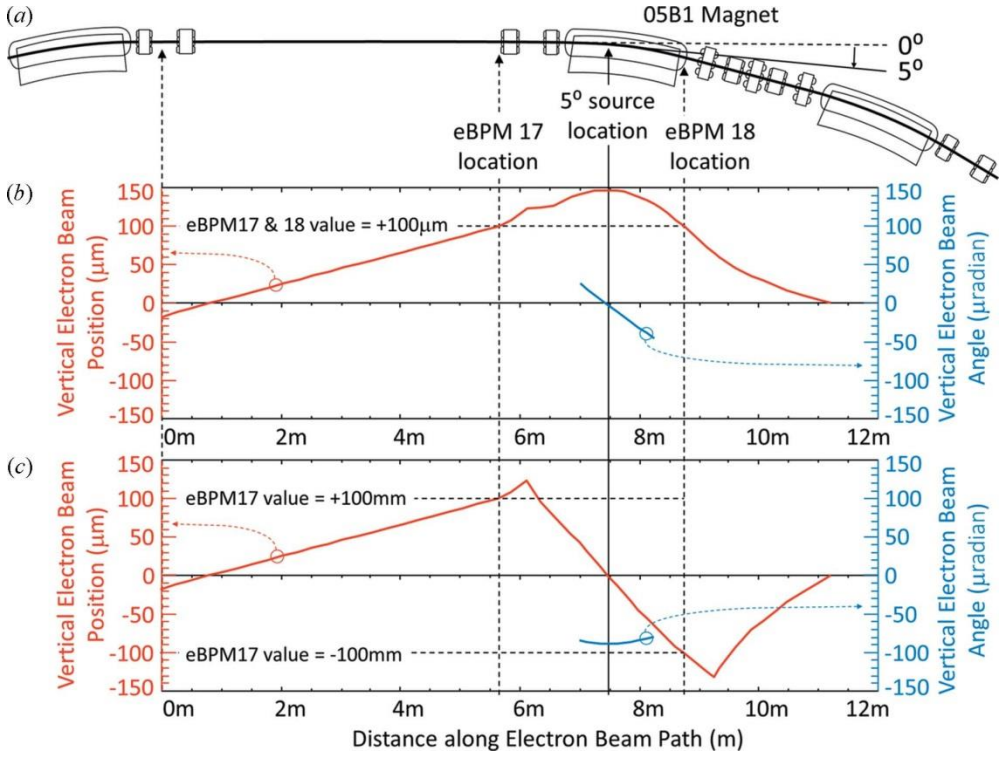

Figure 2- 8 Storage ring schematic and calculated electron beam trajectories. (a) Section of the storage ring around the 05B1 magnet from which the measurements were made. The locations for eBPM17, eBPM18 and 5° source are indicated. The calculated trajectory for +100 μm vertical position for eBPM17 and eBPM18 are shown in (b) with the electron vertical position in red and angle in blue. (c) Trajectory for a +100 μm value at eBPM17 and -100 μm at eBPM18 which mostly creates an angle at the source location.

2.7.1.1 Electron Beam Vertical Position Measurements

For vertical motion the eBPM 17 and eBPM 18 target values were changed by the same amount. The beam was moved vertically between +100 and −100 μm in 0, ±1, ±2, ±5, ±10, ±20, and ±100 μm increments. Examples are shown were the beam is at the zero location (Figure 2- 9 (a)), +100 μm (Figure 2- 9(b)), and −100 μm (Figure 2- 9(c)). In those plots 12 s of beam motion is shown. It should be noted that the measured beam position and angles are relative to the middle of the detector. Three data lines are shown, red, which is the measured electron beam

position, *y*; blue, the electron beam angle multiplied by the distance from the source to the detector, *Dy*' (this allows it to be plotted on the same scale as the position); and purple, the overall beam position, *y*+*Dy*'.

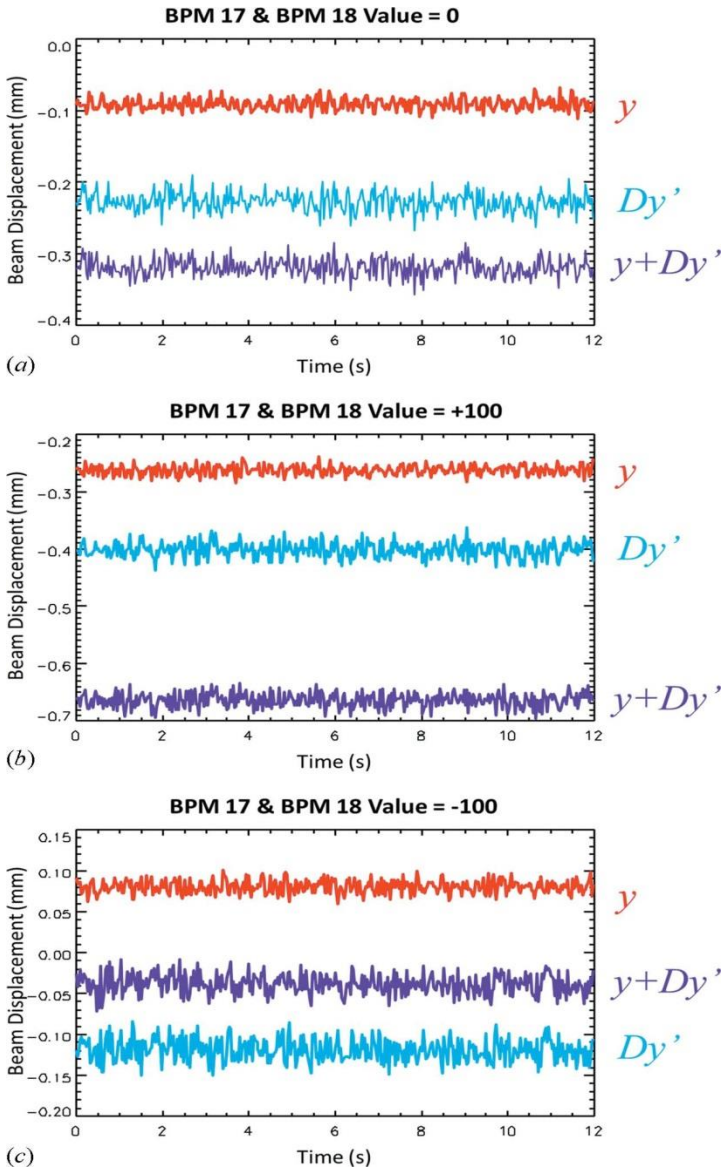

Figure 2- 9 Measurements of the beam vertical position, *y*, the effect of vertical angle, *Dy'*, and combined motion as a function of time for eBPM17/18 values of 0 (a), +100 (b) and -100 (c). The vertical motions have been translated into millimeters using the 100 μm pixel size. The vertical zero is the vertical detector center.

Trends plots of the electron beam position and angle measurements as a function of eBPM offset values are shown in Figure 2- 10 and Figure 2- 11, respectively. Some selected

values are also given in Table 2- 1. The dashed horizontal line in the figures identifies the measured 'zero' location where the electron beam is at the zero location in eBPM units. Clearly, there is good correlation between the eBPM values and the beam position and angle. The red line in Figure 2- 10 and the blue line in Figure 2- 11 are least-squares fits to the measured data. For these data, 150 twelve second measurements (called a "slice") were made as the beam was moved. For each beam location between four and five slices were taken. In reviewing Table 2- 1, the measured standard deviations are in the 10 micron range for y, *Dy'* and *y+Dy'*.

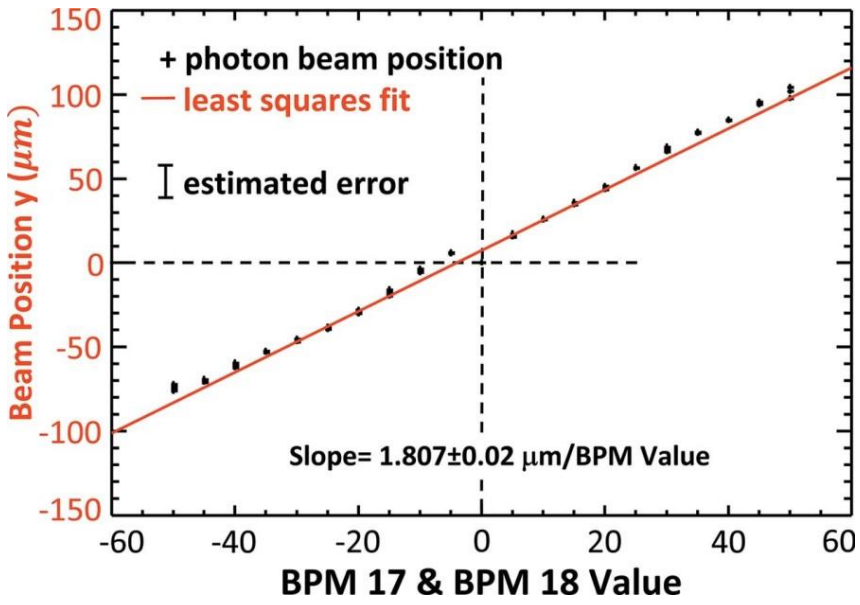

Figure 2- 10 Electron vertical beam position in micrometers measured as the eBPM17 and 18 are changed from -50 to +50 μm.

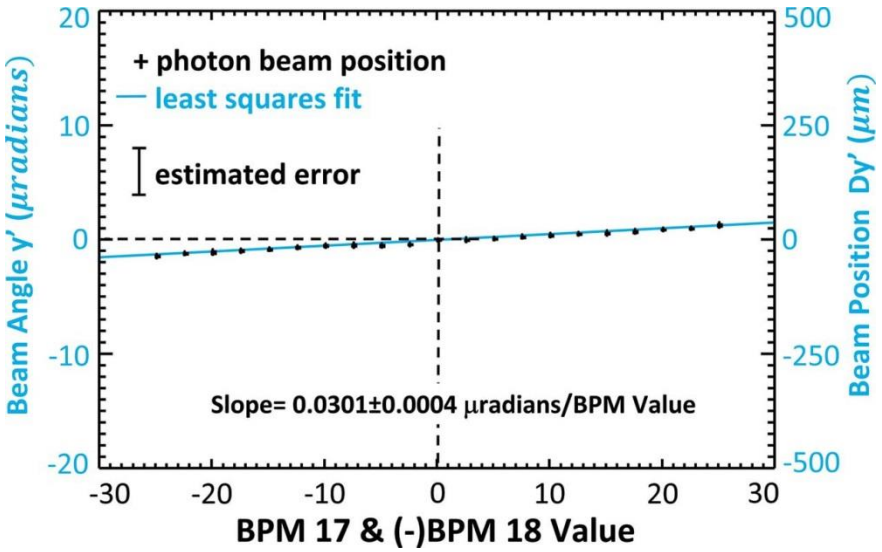

Figure 2- 11 Electron beam vertical angle in microradians measured as the eBPM17 and 18 are changed from -50 to +50 μm. The measured angle in microradians is shown on the left axis and the vertical displacement that angle creates at the detector position, *Dy'*, is shown on the right.

Table 2- 1 Selected measured electron vertical beam position, *y*, and angle, *y'*, as a function of vertical electron beam motion defined by equal eBPM 17 and 18 values.

The slice number identifies the measurement. Columns showing the effect of the electron beam angle on beam position, *Dy'*, and the overall vertical beam motion, *y+Dy'* at the detector, are given along with calculated standard deviations. Each slice corresponds to 12 seconds of acquisition time.

Slice #	BPM 17/18 (μm)	$\bar{y}$ (μm)	$\bar{y}'$ (μrad)	$D\bar{y}'$ (μm)	$\bar{y} + D\bar{y}'$ (μm)
2	0	-401 ± 8	5.89 ± 0.54	146 ± 13	-255 ± 12
82	5	-385 ± 8	6.01 ± 0.56	150 ± 14	-235 ± 12
95	10	-375 ± 8	6.07 ± 0.52	152 ± 13	-223 ± 13
92	20	-356 ± 8	6.34 ± 0.53	158 ± 13	-198 ± 12
99	30	-334 ± 8	6.64 ± 0.55	165 ± 14	-168 ± 13
105	40	-316 ± 8	7.02 ± 0.54	175 ± 14	-141 ± 13
113	50	-297 ± 8	7.34 ± 0.53	190 ± 13	-107 ± 12
121	-5	-396 ± 8	5.45 ± 0.51	136 ± 13	-259 ± 13
125	-10	-406 ± 8	5.34 ± 0.52	133 ± 13	-272 ± 12
133	-20	-430 ± 8	5.24 ± 0.55	131 ± 14	-299 ± 12
139	-30	-448 ± 8	4.97 ± 0.53	124 ± 13	-324 ± 12
146	-40	-461 ± 8	4.52 ± 0.52	113 ± 13	-348 ± 12
153	-50	-467 ± 8	4.16 ± 0.53	103 ± 13	-372 ± 11

From Figure 2- 10, the vertical beam position rate of change was determined to be 1.807 ± 0.02 μm per μm eBPM value from the least-squares fit. From Figure 2- 11, the vertical beam angle rate of change was similarly determine to be 0.0301 ± 0.0004 μrad per μm eBPM value. Based on electron beam optics calculations for an ideal machine, the predicted values should be 1.47 μm per μm eBPM value and -0.034 μrad per μm eBPM value, respectively. The good agreement between the experimentally determined and calculated values is shown in the top row of Table 2- 2.

Table 2- 2 Measured and calculated detector response to vertical electron beam position and angle. Vertical electron beam positions where eBPM17 and 18 are equal are shown in the upper two rows (upper row – measured and lower row – calculated). Vertical beam angle where eBPM17 is equal to, but opposite sign to eBPM18 is shown in the bottom two rows. At the measurement location there is a mixture of position and angle for both types of electron beam motion.

		Position ($\mu rad/\mu m$ offset)	Angle ($\mu rad/\mu m$ offset)
Position Motion	Measured	1.807±0.02	0.0301±0.0004
(eBPM17=eBMP18)	Calculated	1.47	-0.034
Angle Motion	Measured	-0.101± 0.039	-0.842±0.005
(eBPM17= - eBPM18)	Calculated	-0.06	-0.88

2.7.1.2 Electron Beam Vertical Angle Measurements

Similar measurements were made when the eBPM values were changed asymmetrically to create electron beam angle at the beamline. Tests were made with eBPM offsets between +20 and −20 μm in 0, ±5, ±10, ±15, and ±20 increments.

Plots of the electron beam position and angle as a function of eBPM values are shown in Figure 2- 12 and Figure 2- 13, respectively. Some selected values are also given in Table 2- 3 and, as before, the measured standard deviations are in the 10 μm range for *y*, *Dy'* and *y + Dy'*. The dashed horizontal line in the figures identifies the measured zero location where the electron beam is at the zero location in eBPM units. The red line in Figure 2- 12 Electron vertical beam

position in micrometers measured as the eBPM17 and -18 are changed from -20 to +20 μm.Figure 2- 12 and the blue line in Figure 2- 13 are least-squares fits to the measured data.

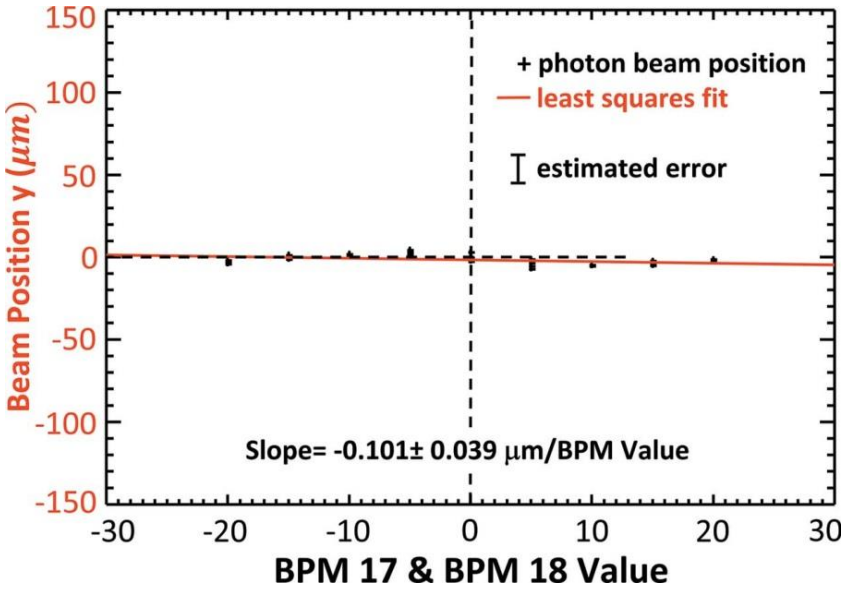

Figure 2- 12 Electron vertical beam position in micrometers measured as the eBPM17 and -18 are changed from -20 to +20 μm.

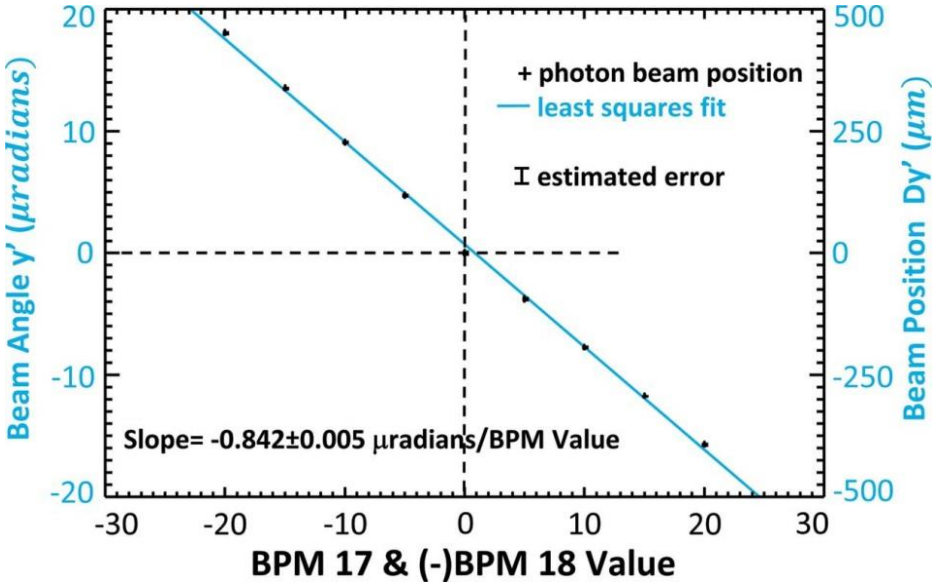

Figure 2- 13 Electron beam vertical angle in microradians measured as the eBPM17 and -18 are changed from -20 to +20 μm. The measured angle in microradians is shown on the left axis and the vertical displacement that angle creates at the detector position, *Dy'*, is shown on the right.

The measured and calculated beam responses are summarized in the lower half of Table 2- 2. Again, there is a good agreement between the measured and ideal machine values.

Table 2- 3 Selected measured electron vertical beam position, *y*, and angle, *y'*, as a function of electron beam angle defined by equal and opposite sign eBPM 17 and 18 values; the remainder of the table is for *Dy'* and *y+Dy'* as defined in Table 2- 1 and in the text.

Slice #	BPM 17/18 (μm)	$\bar{y}$ (μm)	$\bar{y'}$ (μrad)	$D\bar{y'}$ (μm)	$\bar{y} + D\bar{y'}$ (μm)
9	5	-428 ± 8	2.30 ± 0.55	57± 14	-371 ± 14
13	10	-430 ± 8	-1.64 ± 0.51	-41 ± 13	-471 ± 13
20	20	-427 ± 8	-9.63 ± 0.51	-241 ± 13	-667 ± 12
47	-5	-421 ± 8	10.70 ± 0.57	267 ± 14	-154 ± 13
51	-10	-423 ± 8	15.09 ± 0.51	377 ± 13	-46 ± 13
58	-20	-428 ± 8	24.16 ± 0.58	604 ± 15	176 ± 13

2.7.2 Normal Operations Measurements

Measurements with ps-BPM system were made during a number of normal operation shifts between December 2013 and August 2014. During the December 2013 to early 2014 period the CLS storage ring was experiencing beam instabilities from a storage ring dipole magnet power supply.

Figure 2- 14 shows 12 s measurements made during three operational periods in December 2013, March 2014 and August 2014. The top line is the measured electron beam position, *y*, the bottom line is the vertical displacement due to angle, *Dy'*, and the middle line is the sum of two, *y+Dy'*. Each of the three measurement periods are show side by side in the figure. The offsets for the three position types have been removed so that their average is zero to make the comparison easier.

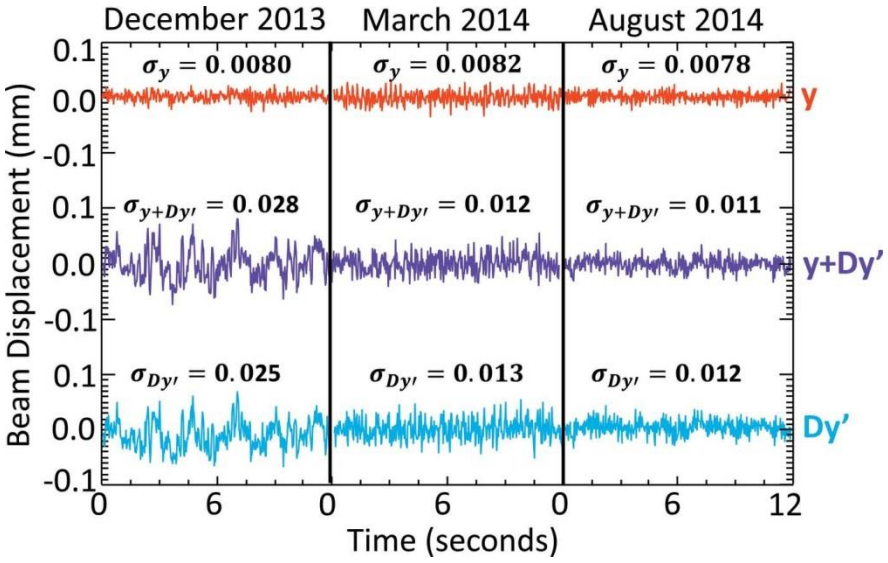

Figure 2- 14 Beam phase-space measurements over a 12 s interval during normal operations for three dates: December 2013, March 2014 and August 2014. The top line is the zero referenced electron beam position, *y*, the bottom line is the vertical displacement due to angle, *Dy'*, and the middle line is the sum of the two, *y + Dy'*. Note the improvement in beam stability over the nine-month period. The standard deviation values are shown above each period.

It is clear that the ring stability improved dramatically during that time period and that the instability measured arose primarily from the angle displacements. The Figure 2- 14 also shows measured standard deviations of the positions, σ_y, $\sigma_{Dy'}$, and $\sigma_{y+Dy'}$. The standard deviation of the electron beam position, σ_y, varied little over the three periods. However, the standard deviation of the vertical displacement due to angle, $\sigma_{Dy'}$, dropped by a factor of two in the same time. The standard deviation of the overall beam displacement due to electron beam positon and angle, $\sigma_{y+Dy'}$, is determined mostly by the electron beam angle.

The DCM could be responsible for some of the measured beam motion due to vibrations and thermal motion. Internal vibrations within the monochromator are somewhat minimized as we used a gravity flow water system for cooling both crystals in the DCM. Also the use of a copper and aluminum filter dropped the incident power on the first crystal to below 2 W for the size of the beam and ring current used for the experiments. Finally, based on our measurements, as the beam is moved in the machine the error bar on the beam displacement was typically less

than 10 μm and the angle less than 0.5 μrad, indicating that the combination of the monochromator and electron beam motions must be less than these values.

2.8 PRACTICAL IMPLEMENTATION OF A PS-BPM

All of the proof-of-principle measurements required the use of the entire beamline and as such would be completely impractical as a monitor. Probably the most challenging aspect of implementing such a monitor would be the dedicated use of the DCM. The complexity of the DCM in which the two crystals must be maintained in sub-microradian alignment in the Bragg geometry could be mitigated by the use of a single-crystal Laue or transmission-type monochromator. The Laue-type monochromator is not so susceptible to crystal heating effects as there is no thermal bump on the crystal's surface. Much of the power can be transmitted through where it can be absorbed elsewhere. The width of the beam being used need not be very wide as two line detectors can be used for the beam and K-edge side measurements. A prototype Laue-type system is being designed.

2.9 CONCLUSIONS

A unique method for simultaneously measuring the vertical position and angle (phase space) of synchrotron photon beams using the combination of x-ray diffraction and absorption edges has been developed and tested at the BMIT beamline at the Canadian Light Source. This system allows the measurement of the photon beam centroid in phase space, and thus the electron beam position and angle, at a single location along the beamline. Temporal stability and beam motion system response measurements have been performed with good results.

The sensitivity of this system is comparable to other photon beam position monitors with detectable position errors on the scale of 10 μm and angle errors of 0.5 μrad. These errors are based on the noise level in the 12 s time measurements of 400 time points.

We are optimistic that a compact dedicated system employing a single transmission or Laue monochromator coupled with a K-edge filter and two line detectors can be built and implemented to make a practical device that uses a small piece of the horizontal width of a bend-magnet or wiggler white beam.

Such a system provides more complete view of beam motion in a synchrotron source and may be used to improve the synchrotron source position and angle stability. The ps-BPM also provides a better diagnostic should instabilities or beam drift occur, and could be used to correct experimental data for beam motion and to actively control the trajectory of the photon beam in the beamline.

2.10 ACKNOWLEDGEMENT

The authors acknowledge the financial support of Canadian Institutes of Health Research (CIHR) Training Grant - Training in Health Research Using Synchrotron Techniques (NS, MM, BB), Saskatchewan Health Research Foundation Team Grant (NS, DC), Natural Sciences and Engineering Research Council of Canada (NSERC) Discovery Grant (DC), the University of Saskatchewan (NS, MM), and Canada Research Chair Program (DC). Research described in this paper was performed at the Canadian Light Source, which is funded by the Canada Foundation for Innovation, NSERC, the National Research Council Canada, CIHR, the Government of Saskatchewan, Western Economic Diversification Canada, and the University of Saskatchewan.

2.11 REFERENCES

1. Brefeld, W., Stabilization of synchrotron radiation beam at HASYLAB (invited). Review of Scientific Instruments, 1989. **60**(7): p. 1513-1516.
2. K. Haga, et al. The Vibration Measurements at the Photon Factory Storage Ring Building. in European Particle Accelerator Conference. 2000. Vienna, Austria.
3. Galimberti, A. and R. Borghes, Operational Experience with the Photon Beam Position Monitor for Undulator Beamlines of Elettra. AIP Conference Proceedings, 2004. **705**(1): p. 584-587.
4. Rehm, G., Achieving and Measuring Sub-Micrometer Beam Stability at 3rd Generation Light Sources. Journal of Physics: Conference Series, 2013. **425**: p. 042001.
5. Hettel, R., Review of synchrotron beam stability and stabilizing systems (invited). Review of Scientific Instruments, 1989. **60**(7): p. 1501-1506.
6. Bocchetta, C.J. Lifetime and beam quality. in CAS - CERN Accelerator School 1996. Grenoble, France.
7. Farvacque, L. Beam Stability. in CAS - CERN Accelerator School. 1996. Grenoble, France.
8. Hettel, R.O., Beam stability at light sources (invited). Review of Scientific Instruments, 2002. **73**(3): p. 1396-1401.
9. Billing, M.G., Beam position monitors for storage rings. Nuclear Instruments and Methods in Physics Research Section A: Accelerators, Spectrometers, Detectors and Associated Equipment, 1988. **266**(1–3): p. 144-154.
10. Izumi, T., T. Nakajima, and T. Kurihama, Photon beam position monitor. Review of Scientific Instruments, 1989. **60**(7): p. 1951-1952.
11. Johnson, E.D. and T. Oversluizen, Compact high flux photon beam position monitor. Review of Scientific Instruments, 1989. **60**(7): p. 1947-1950.
12. van, R., A high-precision X-ray beam-position and profile monitor for synchrotron beamlines. Journal of Synchrotron Radiation, 1999. **6**(6): p. 1071-1075.
13. Alkire, R.W., G. Rosenbaum, and G. Evans, Design of a vacuum-compatible high-precision monochromatic beam-position monitor for use with synchrotron radiation from 5 to 25 keV. Journal of Synchrotron Radiation, 2000. **7**(2): p. 61-68.
14. Kyele, N.R., K. Decanniere, and R.G. van Silfhout, A transparent two-dimensional in situ beam-position and profile monitor for synchrotron X-ray beamlines. Journal of Synchrotron Radiation, 2005. **12**(6): p. 800-806.
15. Bunk, O., et al., X-ray beam-position monitoring in the sub-micrometre and sub-second regime. Journal of Synchrotron Radiation, 2005. **12**(6): p. 795-799.

16. Bergonzo, P., D. Tromson, and C. Mer, CVD diamond-based semi-transparent beam-position monitors for synchrotron beamlines: preliminary studies and device developments at CEA/Saclay. Journal of Synchrotron Radiation, 2006. **13**(2): p. 151-158.

17. Ilinski, P., et al., Residual Gas X-ray Beam Position Monitor Development for PETRA III. AIP Conference Proceedings, 2007. **879**(1): p. 782-785.

18. Tucoulou, R., et al., High-resolution angular beam stability monitoring at a nanofocusing beamline. Journal of Synchrotron Radiation, 2008. **15**(4): p. 392-398.

19. Leban, P., D. Tinta, and C. Pradervand. Photon Beam Position Measurements using CVD Diamond based Beam Position Sensor and Libera Photon at Swiss Light Source. in International Particle Accelerator Conference. 2010. Kyoto, Japan.

20. Revesz, P., A.B. Temnykh, and A.K. Pauling, New X-ray beam position monitors with submicron resolution utilizing imaging of scattered X-rays at CHESS. Nuclear Instruments and Methods in Physics Research Section A: Accelerators, Spectrometers, Detectors and Associated Equipment, 2011. **649**(1): p. 94-96.

21. Xiao, Y., et al., Development of a PSD-based photon beam position measurement system. Nuclear Science and Techniques, 2012. **23**: p. 70-74.

22. Muller, E.M., et al., Transmission-mode diamond white-beam position monitor at NSLS. Journal of Synchrotron Radiation, 2012. **19**(3): p. 381-387.

23. Cheng, X.C., et al., V-coupling-blades beam position monitor for NSRL undulator source. Journal of Physics: Conference Series, 2013. **425**.

24. Kachatkou, A. and R. van Silfhout, On the resolution and linearity of lensless in situ X-ray beam diagnostics using pixelated sensors. Opt Express, 2013. **21**(4): p. 4291-302.

25. Hahn, U., et al., Beam-position monitors in the X-ray undulator beamline at PETRA. Journal of Synchrotron Radiation, 1998. **5**(3): p. 627-629.

26. Kyele, N.R., et al., In situ synchrotron x-ray photon beam characterization. Journal of Applied Physics, 2007. **101**(6): p. 064901.

27. Morse, J., B. Solar, and H. Graafsma, Diamond X-ray beam-position monitoring using signal readout at the synchrotron radiofrequency. Journal of Synchrotron Radiation, 2010. **17**(4): p. 456-464.

28. Bergstrom, J.C. and J.M. Vogt, The optical diagnostic beamline at the Canadian Light Source. Nuclear Instruments and Methods in Physics Research Section A: Accelerators, Spectrometers, Detectors and Associated Equipment, 2006. **562**(1): p. 495-512.

29. Thompson, A., X-Ray Data Booklet, D.o. Energy, Editor. 2009, Lawrence Berkely Laboratory: Berkeley, CA USA.

30. Golovchenko, J.A., R.A. Levesque, and P.L. Cowan, X-ray monochromator system for use with synchrotron radiation sources. Review of Scientific Instruments, 1981. **52**(4): p. 509-16.

31. DuMond, J.W.M., Successive x-ray crystal reflections to obtain increased resolving power. Physical Review, 1937. **52**: p. 872-883.

32. Feiters, M.C., F.C. Kupper, and W. Meyer-Klaucke, X-ray absorption spectroscopic studies on model compounds for biological iodine and bromine. Journal of Synchrotron Radiation, 2005. **12**(1): p. 85-93.

CHAPTER 3

CONCLUSION AND FUTURE DIRECTIONS

3.1 CONCLUSION

A unique method and system for simultaneously measuring the vertical position and angle (location in phase space) of synchrotron photon beams using the combination of x-ray diffraction and absorption edges has been developed and tested at the biomedical beamline (05B1-1) at the Canadian Light Source. The double crystal monochromator (DCM) on this beamline which uses a (2,2,0) silicon reflection was used to prepare a beam around the absorption edge of iodine at 33.169 keV. The vertical divergence of the photon beam onto this monochromator gave a variable range of energies that encompassed the iodine K-edge energy due to the range of angles onto the lattice planes of the DCM crystals. Without the iodine filter a measurement of the vertical photon beam position will give the combination of the electron beam's position and angle. With the iodine filter a measurement of the vertical location of the K-edge will give the electron beam's vertical position. From these two measurements with and without the filter this system allows the determination of the photon beam phase space position, and thus the electron beam phase space position at a single location along the beamline.

There were two types of measurements done to test the sensitivity and functionality of the system as well as using the system to measure the storage ring electron beam stability. Several 8-hour shifts during machine studies and normal operations were used for these measurements. Comparison between results from the data taken during machine study shifts and the values that was predicted by an "ideal machine" calculation showed good agreement. The ideal machine

calculations were done using an electron beam optical program called DIMAD [1]. These calculations coupled with measurements gave a great deal of confidence that the system was working as expected and should be pursued as a measurement tool. To this end, the system was used during normal operations to measure the beam stability. Measurements were done during a time period when the beam stability was affected by a faulty dipole magnet power supply. These measurements along with later measurements when the problem was fixed, clearly demonstrated the improvement in stability.

The sensitivity of this system is comparable to other PBPMs with position errors on the scale of 10% of the vertical beam size and angle. At the CLS this corresponds to roughly 10 microns in position and angle errors of 0.5 microradians. These errors are based on the noise level in the 12 second time measurements of 400 time points.

Such a system provides a more complete view of beam motion with a synchrotron source and may be used to improve source stability, provide a better diagnostic should instabilities occur, could be used to correct experimental data for beam motion and to actively control the trajectory of the photon beam in the beamline.

3.2 FUTURE WORK

I feel that this system will be able to measure the electron beam vertical phase space position and should be pursued. However there may be more information than has been presented in this thesis that can be extracted from the data. Also to be practical a system would need to be built that would not require the use of an entire beamline for these measurements. These two areas of research and development need to be pursued.

3.2.1 Extracting more information from the measurements

The analysis that has been applied used several kinds of algorithms to extract information from the data. The fits of the algorithm included an amplitude, a center location, a background value and a width parameter. For the purposes of the paper and this thesis only the center location from the algorithm was used to determine the beam phase space position. The amplitude and the background value are just the measurements of the intensity of the beam or the absorption of the filter. However the width is a measure of the intrinsic properties of the photon and electron beam position and angle distribution coupled with the physical properties of the filter and the geometry of the arrangement of the system. For example, the vertical size of the measured photon beam at some distance from the source should be the combination of the electron beam's vertical size and vertical range of angles coupled with the intrinsic opening angle of the photon beam from a single electron source. The measured width of the K-edge of a filter element should be the combination of the electron beam's vertical size coupled with the intrinsic K-edge width of the element. Extracting the electron beam's size and angle from these two width measurements is a topic that must be pursued as it gets at one of the most fundamental properties of the source itself – the emittance.

The emittance is a property of the electron beam within the storage ring and is a measure of the average spread of the electron beam's location in phase space. A low vertical emittance electron beam has the electrons confined to a small vertical size and a small range of vertical angles. For the storage ring, low emittance means that the resulting x-ray beam will be small, which results in higher brightness [2].

I believe that I can measure the vertical emittance using the ps-BPM system. It might also be possible to measure some aspect of the horizontal emittance using a horizontally placed system. Determining the use of this system for emittance measurements is a topic of future study

and should be done in coordination with altering the storage ring properties to validate this concept.

3.2.2 The system

I am optimistic that a compact dedicated system employing a single transmission or Laue monochromator coupled with a K-edge filter and two line detectors can be built and implemented to make a practical device that uses a small piece of the horizontal width of a bend magnet or wiggler white beam.

For the proof of principle measurements, an entire beamline was used. Obviously, to be a practical system, a less invasive method would be needed. The critical pieces of the system are

1. The monochromator
2. The filter assembly
3. Two position sensitive detectors or an area detector

To be minimally invasive on the synchrotron photon beam the ps-BPM should be located in a place where there would be access to an edge of the photon beam and would use a few millimeters of the beam width. To avoid changes in the system response due to beamline operational conditions it should be located upstream of variable slits or filters.

The system should be vacuum compatible and compact so that it can be placed in a beamline with minimal difficulty in terms of complexity and space. Additionally, the electronic components of the system should be radiation hardened and/or be protected from excessive radiation exposure.

To be usable as a monitor or in a feedback control application, the detection and data processing should be real–time or near real–time. Finally, for general applicability the overall

system cost should be low, the initial alignment should be straight-forward, the operation and the recalibration simple.

3.2.3 Applications

As noted earlier the applications are:

1. For electron beam diagnostics (electron beam position / angle / emittance).
2. As a feedback element for stabilizing the electron or the photon beam.
3. A source of additional information that when used with the acquired experimental data can be used to correct for errors caused by the photon beam motion.

The first two applications for diagnostics and feedback are straightforward but the third use for data correction could open up new approaches to improve experimental results beyond that which is currently feasible.

For many experiments the fact that the beam may move due to position or angle may have no impact on the quality of the data as it can be easily corrected. However for spectroscopy research the beam angle through the monochromator will introduce photon energy errors that cannot be corrected without knowledge of the beam angle. For example, as noted earlier in the Introduction in one of the Spectral KES experiments we saw horizontal bandings in the images that indicated that the photon beam is moving. It was also noticed when the beam moved the location of the K-edge moved a different amount. The normal approach to removing banding by using the left and right the edges of the beam to renormalize each image line to remove vertical intensity variations (horizontal banding) would not account for a different location of the K-edge in each horizontal line. The Spectral KES algorithm relies on a constant location of the K-edge for successful extraction of the contrast image from the water image. K-edge motion will affect the fitting of the experimental data to the measured or calculated K-edge structure of the contrast

agent, thus introducing noise. Independent knowledge of the beam phase space position would allow for a more accurate results.

Finally, there may be other synchrotron research techniques that may benefit from independent knowledge of the electron or photon beam phase space position being used to correct or improve the quality of the data.

As a closing note, a proposal for beamtime on the 1BM beamline at the Advanced Photon Source (APS) at Argonne National Laboratory near Chicago was accepted and scheduled for February 2016 to test this approach at that facility. That beamtime is coordinated between storage ring normal operations and machine studies so that similar measurements could be done. There is interest in this system at that facility because of an upcoming upgrade which will improve dramatically the brilliance and beam stability will become much more important. The information provided by this system could provide more insight into the storage ring performance.

3.3 REFERENCES

1. Servranckx RV. Users Guid to the Program DIMAD. 1990.
2. Thompson A. X-Ray Data Booklet. In: Energy Do, editor. rev 3 ed. Berkeley, CA USA: Lawrence Berkely Laboratory; 2009.

APPENDIX A

A.1 DATA COLLECTION SHIFTS

Two different types of shifts were used to collect data for this experiment, one during special shifts which the beam was moved in vertical position or angle, and the other during the facility's normal operations.

Table A- 1 shows details about the experiments that were performed.

Table A- 1 Detailed description of data collection shifts.

Date	Duration	Shift Type	Reflection	K-Edge Element	Folder Number	Images per Folder	Beam Filters
13 Dec 2013	1 shift	Normal Ops	(2,2,0)	iodine (33.17keV)	480	400	0.276mm Cu
14 Dec 2013	1 shift	Normal Ops	(4,4,0)	Iodine (33.17keV)	370	720	0.276mm Cu
20 Feb 2014	1 shift	Normal Ops	(2,2,0)	Iodine (33.17keV)	270	400	0.276mm Cu
21 Feb 2014	1 shift	Normal Ops	(4,4,0)	Iodine (33.17keV)	268	400	0.276mm Cu
6 Mar 2014	1 shift	Normal Ops + Wiggler ON	(2,2,0)	Iodine (33.17kev)	199	400	0.276mm Cu + 0.110mm Al
11 Mar 2014	1 shift	DS Shift	(2,2,0)	Iodine (33.17keV)	300	400	0.276mm Cu + 0.110mm Al
18 Mar 2014	1 shift	NS Shift	(2,2,0)	Iodine (33.17keV)	152	400	0.276mm Cu + 0.110mm Al
19 Aug 2014	1 shift	Normal Ops	(2,2,0)	Iodine (33.17keV)	20	400	0.276mm Cu + 0.110mm Al

13 Jan 2015	1 shift	DS shift	(2,2,0)	Iodine (33.17keV)	194	400	0.276mm Cu + 0.110mm Al
19 Jan 2015	1 shift	DS shift	(2,2,0)	Iodine (33.17keV)	164	400	0.276mm Cu + 0.110mm Al

Data was collected in different modes of the facility operations: Normal Operation (current 250 mA), Development mode (DS) special beamline development (senior operator and health, safety & environment support) and Normal mode special beamline requests/commissioning (NS). For contrast element some data were taken with molybdenum filter but because the study was focused on iodine K-edge it's not included. The folder number indicates how many folders of images were taken in that shift.

APPENDIX B

B.1 FITTING ALGORITHMS

To find a suitable fitting algorithm to analyze the K-edge region of data (this will be called edge data), a number of fitting algorithms were explored. Some were chosen because of their simplicity to implement while others were chosen because they may better represent the shape of the iodine absorption edge. There were a number of metrics that were looked at to try to establish which method might better represent the location of the K-edge which was the goal of the fitting exercise. The metrics are, (1) being able to fit, without failure, most or all of the data acquired, (2) comparing the standard deviation of the fits of the edge location against the other methods, (3) goodness (chi-squared) of fit between the data and the fitting function, and (4) if the fitting function makes physical sense.

There are three functional types that were investigated; Gaussian (G), Lorentzian (L) and Pseudo-Voigt (V). The fit can either be to the edge data which looks like a step function or the derivative of the edge data which will be a peak. If the edge data is fit we use the integral versions of the three functional types (I). If the derivative of the edge data is fit we used the functions as they are (D). Finally, the edge data can be the raw data as acquired or the negative logarithm of that raw data to convert it into an absorbance (Linear attenuation coefficient times thickness). Thus, there are two choices for the edge data to be processed prior to fitting; the raw data or no logarithm (N) and the negative logarithm of the raw data (L). Therefore, there are twelve ways to fit the data: (three functional types, [G,L,V]) X (non-derivative or derivative of the edge data, [I,D]) X (logarithm or no logarithm of the raw data, [L,N]). This is summarized in Table B- 1.

Table B- 1 Summary of different types of fitting algorithms and the pre-processing of the data used

Function	Integral/Derivative	Log/ No Log
Gaussian – G Lorentzian - L Pseudo-Voigt - V	Integral – I Derivative – D	Logarithm – L No Logarithm - N

For clarity, those fits are listed below:

1. An error function fit to the negative logarithm of the averaged edge line data. This error function is simply an integral of a Gaussian function. The negative logarithm will convert the averaged edge line data into "μt" values. [GIL]
2. An error function fit to the averaged edge line data. No logarithm of the data was taken. [GIN]
3. A derivative of the negative logarithm of the averaged edge line data was taken to convert the edge jump into a peak. A Gaussian was then fit to this peak. [GDL]
4. A derivative of the averaged line data was taken (NO negative logarithm was taken) and a Gaussian function was used to fit the peak. [GDN]
5. Similar to the error function fits earlier a more physical function (Lorentzian) was used to fit the data. An integrated Lorentzian function was used to fit the negative logarithm of the averaged edge line data. [LIL]
6. An integrated Lorentzian fit was done to the averaged edge line data (no logarithm was used). [LIN]

7. A Lorentzian fit was made to the derivative of the negative logarithm of the averaged edge line data. [LDL]
8. A Lorentzian fit was made to the derivative of the averaged edge line data. [LDN]
9. Similar to the error function fits earlier a Pseudo-Voigt function (Lorentzian + Gaussian) was used to fit the data. An integrated Pseudo-Voigt function was used to fit the negative logarithm of the averaged edge line data. [VIL]
10. An integrated Pseudo-Voigt fit was done to the averaged edge line data (no logarithm was used). [VIN]
11. A Pseudo-Voigt fit was made to the derivative of the negative logarithm of the averaged edge line data. [VDL]
12. A Pseudo-Voigt fit was made to the derivative of the averaged edge line data. [VDN]

APPENDIX C

C.1 DATA PROCESSING PROGRAMS

Two main programs were developed in IDL (Interactive Data Language, Excelis Visual Information Solutions, Boulder, CO USA) to process the image data. The first one, "ANALYZE_BEAM_MULTI_FIT":

1. Reads the image data
2. Extracts the beam side profile from each of the image data files
3. Fits the beam side profile with a Gaussian function
4. Extracts the edge side profile from each of the image data files
5. Normalizes that profile with the flat image data
6. Fits the edge side with
    a. Integrated Gaussian fit to the logarithm of the edge profile (GIL,1)[1]
    b. Integrated Lorentzian fit to the logarithm of the edge profile (LIL,2)
    c. Integrated pseudo-Voigt fit to the logarithm of the edge profile (VIL,3)
    d. Integrated Gaussian fit to the edge profile (GIN,4)
    e. Integrated Lorentzian fit to the edge profile (LIN,5)
    f. Integrated pseudo-Voigt fit to the edge profile (VIN,6)
    g. Gaussian fit to the derivative of the logarithm of the edge profile (GDL,7)
    h. Lorentzian fit to the derivative of the logarithm of the edge profile (LDL,8)
    i. Pseudo-Voigt fit to the derivative of the logarithm of the edge profile (VDL,9)
    j. Gaussian fit to the derivative of the edge profile (GDN,10)
    k. Lorentzian fit to the derivative of the edge profile (LDN,11)

[1] The number refers to an index used in the subsequent analysis program.

l. Pseudo-Voigt fit to the derivative of the edge profile (VDN,12)

7. Saves the fit information for each of the image data files into a single IDL "DAT" file.

The program is run in the following way,

```
IDL> b=analyze_beam_multi_fit( beam=[300,400], edge=[600,700])
```

The numbers in the brackets identify the horizontal pixel range for the beam and edge regions in all of the image files. Each range is 101 pixels wide. Figure C- 1 shows an example of the area that was chosen for one data set.

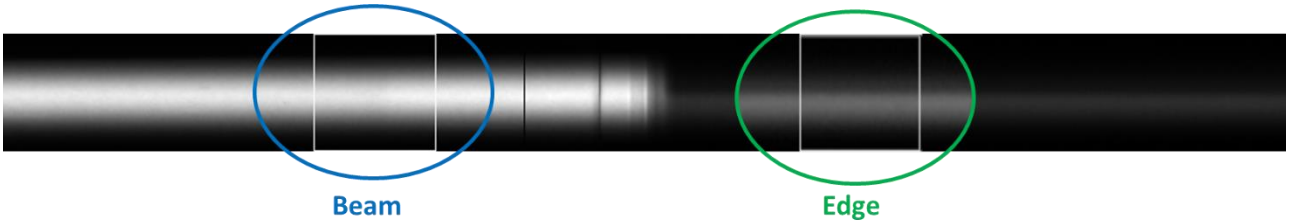

Figure C- 1 Example data image. Regions are chosen from both image types for beam and edge analysis. The edge region is enhanced to better show the K-edge.

This program calls a number of other routines. The routines that fit the beam and the edge profiles are highlighted in yellow in the following listing:

```
IDL> b=analyze_beam_multi_fit( beam=[600,700], edge=[300,400])
% Compiled module: ANALYZE_BEAM_MULTI_FIT.
% Compiled module: READ_AVERAGE_TIFS.
% Compiled module: BEAM_EDGES.
% Compiled module: GAUSSFIT.
% Compiled module: CURVEFIT.
% Compiled module: FIND_TIFF_TIME.
% Compiled module: PARSE.
% Compiled module: FWHM.
% Compiled module: INTERPOL.
% Compiled module: GAUSSFITTER.
% Compiled module: DERIV.
% Compiled module: INT_GAUSSFIT.
% Compiled module: INT_LORENTZFIT.
% Compiled module: INT_PSEUDO_VOIGTFIT.
% Compiled module: LORENTZFIT.
% Compiled module: PSEUDO_VOIGTFIT.
```

The second program, "ANALYZE_ALL_BEAM_MOTION_SLICES_MULTI_FIT":

1. Reads the IDL "DAT" file that was created with the first program

2. Creates a single “csv” file for each fit type

3. Saves them in a single folder

4. Creates plots for each fit type

5. Saves them in separate folders according to the fit type.

The program is run in the following way (the number 6 indicates the fit type to be analyzed, GDL=6)

```
IDL> analyze_all_beam_motion_slices_multi_fit, dat, 6
% Compiled module: ANALYZE_ALL_BEAM_MOTION_SLICES_MULTI_FIT.
% Compiled module: BEAM_MOTION_DIR_MULTI_FIT.
% Compiled module: BEAM_MOTION_DAT_MULTI_FIT.
% Compiled module: STDEV.
```

An Example of a plot created by the program is shown in Figure C- 2.

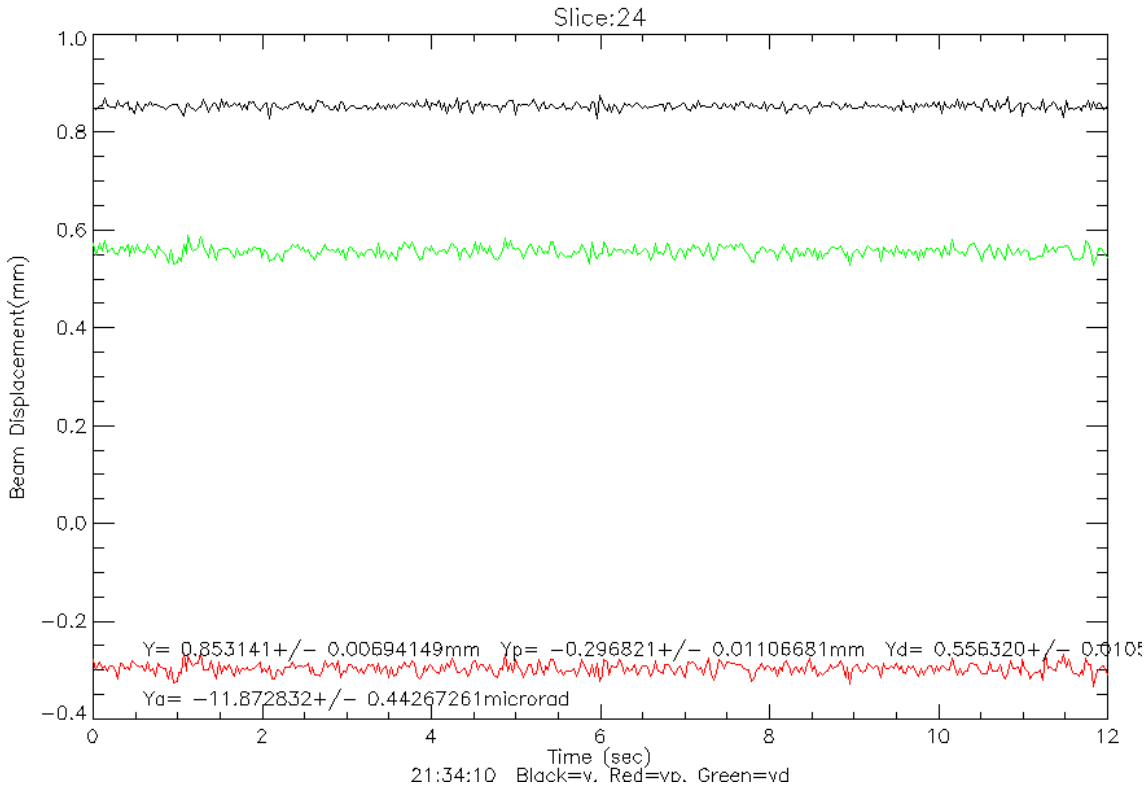

Figure C- 2 Measurements of the beam vertical position, y (black), the effect of vertical angle, Dy’ (red), and combined motion as a function of time, y+ Dy’ (green). The vertical motions have been translated into millimeters using the 100 μm pixel size. The vertical zero is the vertical detector center.

An example of the excel file created by the program is shown in Figure C- 3.

Figure C- 3 Example Excel compatible Comma Separated Values (CSV) output file of the "analyze_all_beam_motion_slices_multi_fit" procedure.